Appendix to RR384

Numerical modelling of the rutting and pavement response with non-uniform tyre/pavement contact stress distributions

Research report

Dr Sabine Werkmeister, Technische Universitaet Dresden, Germany
Dr Martin Gribble, Opus Central Laboratories, Wellington, New Zealand

18 September 2009

Contents

1 Introduction

Asphalt pavements have traditionally been designed using empirical design methods, ie the material types and layer thicknesses of the different structural layers have been selected in accordance with inflexible predetermined design criteria. A typical feature of many empirical design methods is that they have been progressively calibrated over many years, by means of either systematic road tests or observations made from actual road structures. As a result, the design and construction of the pavements have conventionally been directed towards more or less standardised cross sections and road construction materials.

Nonetheless, there are increasing worldwide efforts towards developing mechanistic approaches. The mechanistic design methodology aims to model the behaviour of each pavement layer based on the basic mechanical and physical properties of the structural materials. The key idea is to evaluate the stresses and strains under real traffic loads at critical points in the structure based on the analysis of the stress-strain conditions of the whole pavement. Knowing the values of stresses and strains, the service life of the pavement can be estimated, theoretically more accurately compared to the traditional design approaches.

Computer programs are typically used for mechanistic pavement design. Within the design process the pavement response under traffic loads is calculated using multilayer theory programs (eg CIRCLY or BISAR) or using finite element (FE) programs. Compared with multilayer-based programs, FE programs are able to model the pavement performance more accurately by taking into account the non-linear elastic and plastic performance of the pavement materials. Hence, the advantage of using FE programs is that, for example, the stress-dependent behaviour of the materials can be considered within the pavement design process.

A pre-requisite for any successful mechanistic pavement design is the acquisition of reliable measurements from representative experimental investigations and the appropriate mathematical characterisation of the tyre/pavement stress interaction producing deformation in the layers.

Traditionally pavement design has assumed a simplified tyre/pavement contact stress distribution with a uniform vertical stress at the tyre/pavement interface. This approach is usually adequate for thicker asphalt pavements (> 50mm asphalt layer thickness) but is highly inaccurate for pavements with thinner layers (see for example De Beer (1996)). Because most New Zealand roads have thin pavements the consideration of the actual non-uniform tyre/pavement contact stress distribution is of critical importance to ensure the accurate quantification of the actual stresses and strains in the pavement. Horizontal stresses in the pavement resulting from non-uniform contact stress distribution can be much higher compared with the pavement stresses computed using an assumed uniform vertical contact stress distribution (Tielking et al 1987). Special computer programs (eg developed by Park (Park et al 2005)) or the approaches created by Groenendijk (1998) are available to predict the vertical, longitudinal and transverse tyre/pavement contact stresses for selected tyre configurations. Furthermore, it was found that the complex non-uniform tyre/pavement contact stress distribution can only be properly taken into account by means of FE or Distinct Element programs.

1.1 Objectives

One of the main objectives of the current research work was to use both the non-uniform tyre/pavement contact stress as well as the uniform contact stress distribution in numerical models (FE) in order to determine the effect of the more accurate contact stress distribution on the pavement

response and rutting performance. In addition, the comparison of the uniform and non-uniform stress distribution was conducted in an attempt to establish how the current simplified approach may be used to provide a better approximation of the pavement response for pavement design.

Because a thin surfacing layer, typical of New Zealand pavements, does not have a significant effect on the pavement response in terms of the load distribution and rutting performance, the unbound base course layer plays the most important role for the mechanical response of the pavement. Hence, the research work detailed in this report was primarily focused on the elastic and plastic performance of the granular layer due to the uniform and measured non-uniform tyre/pavement contact stress distributions. The 3D-FE Program ReFEM developed by Oeser (2004), including a non-linear elastic model for unbound granular materials (UGM), was used for the investigation.

The input for the computer models was derived from full-scale load testing carried out at Transit NZ's (now NZTA) CAPTIF full-scale indoor pavement test facility in Christchurch, New Zealand. A full treatment of the apparatus, instrumentation, and test procedures has been given in Douglas et al (2008). In summary, a purpose-built instrument with a linear array of 25 vertical strain-gauged pins, spaced at 25mm centres, was placed in the pavement, flush with the pavement surface. The pins sensed vertical, longitudinal and transverse loading across the width of the tyre(s). Pin load data was collected for single and dual tyre wheels, loaded to 40 or 50kN, with inflation pressures of 280, 550 or 690kPa.

2 Characterisation of tyre footprint contact stress as an input into the FE program ReFEM

The tyre load data provided was derived experiments using single and dual-tyred wheels, two wheel loads (40 kN and 50 kN) and two tyre inflation pressures (280 or 550kPa and 690kPa). The test designations shown in table 1 were adopted.

Table 1 Experiment test designations

Test designation	Wheel	Wheel load (kN)	Tyre inflation pressure (kPa)
S40550	Single tyre	40	550
S40690			690
S50550		50	550
S50690			690
D40280	Dual tyre	40	280
D40690			690
D50280		50	280
D50690			690

The curves displayed in figure 1 to figure 12 show the raw data for the vertical, transverse and longitudinal pin loads measured by the apparatus. The tyre widths and tyre lengths assumed are shown in table 2.

Table 2 Tyre dimensions

Abbreviation	Tyre contact width [mm]	Tyre contact length [mm]	Contact area [mm²]
S40550	250	330	82,500
S40690	250	310	78,000
S50550	250	360	90,000
S50690	275	310	84,200
D40280	250/250	370	186,000
D40690	250/275	280	147,000
D50280	250/250	410	203,000
D50690	275/250	300	159,000

From the values presented in table 2 it is clear that when the load increases the tyre/pavement contact area increases as well. For the vertical loading, symmetry was assumed. The regions that exhibit similar behaviour have been averaged.

Because the FE program used limited the number of elements that were available for loading the contact area was set at 6 elements wide by 9 elements long. For single tyres, the 11 load records were reduced to nine strips using the averaging processes described below. The time record was divided into six sections to represent the length of the tyre as it travelled over the pins. The final load value assigned to each tyre contact element was the average of approximately 200 time samples, with the actual length being determined by the length of the total record.

The final vertical stress was generated by assuming that the stress applied to the pin was in effect applied to area one sixth by one ninth the area of the tyre footprint. This resulted in discontinuities in the stress applied to the pavement, a consequence of the discrete nature of the FE method used in the modelling process.

The separation of the pins by 25mm in the linear array in the apparatus meant that the transverse stress profile was undersampled and the precise profile could not be determined from the available data. In addition, as shown in table 11, with the 25mm pin spacing, the identification of the tyre width from the number of pins recording a load is open to a variation of as much as 50mm. Furthermore, not all the pins output non-zero readings for the same length of time because the centre of the tyre was in contact with the pavement longer than the edges. The length of the record was shortened to the length of the shortest record. Vehicle speed was approximately 10km/hr and this value was used to convert the time records into tyre contact positional values.

2.1 S50550

Figures 1 to 3 show the measured pin loads for a wheel load of 50kN and a tyre inflation pressure of 550kPa. The tyre width spanned 11 pins (pins 12–22) for S50550. The observed vertical pin loadings were averaged as indicated in table 3 and then nine loading strips were generated as indicated in table 4. These strips were then each further divided into six elements longitudinally. Thus the measured tyre vertical, longitudinal and transverse loads were converted into 9 (transversely) × 6 (longitudinally) x 3 (stress directions) element values.

Figure 1 Recorded vertical pin loading on a single tyre with a 50kN wheel load and tyre inflation pressure of 550kPa

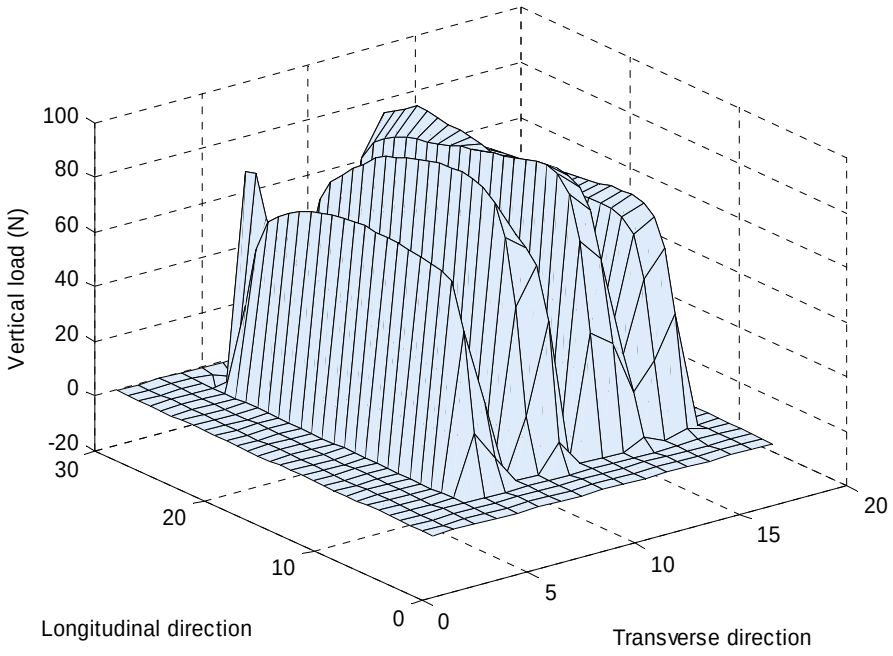

Figure 2 Recorded longitudinal pin loading on a single tyre with a 50kN wheel load and tyre inflation pressure of 550kPa

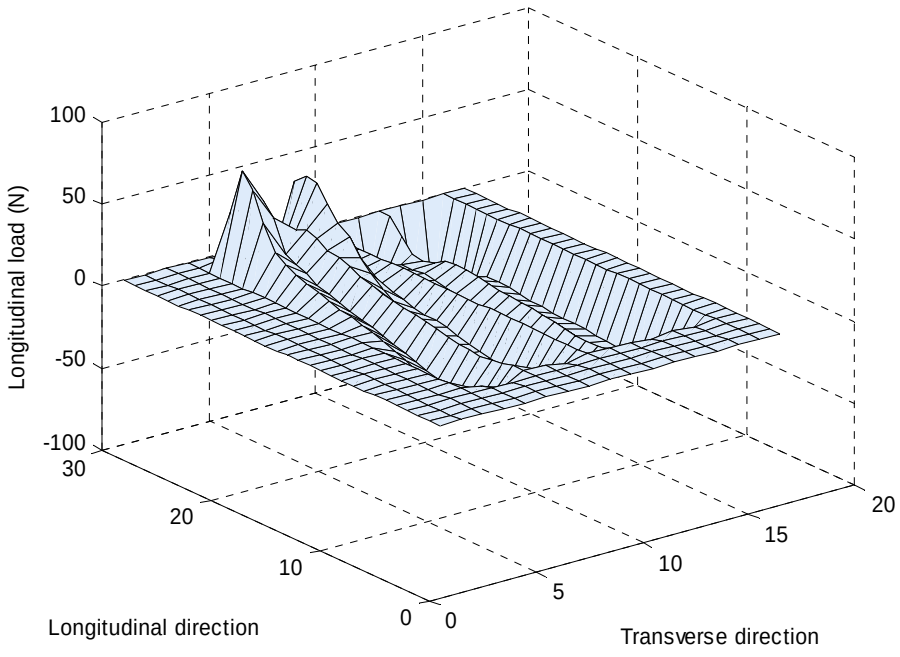

Figure 3 Recorded transverse pin loading on a single tyre with a 50kN wheel load and a tyre inflation pressure of 550kPa

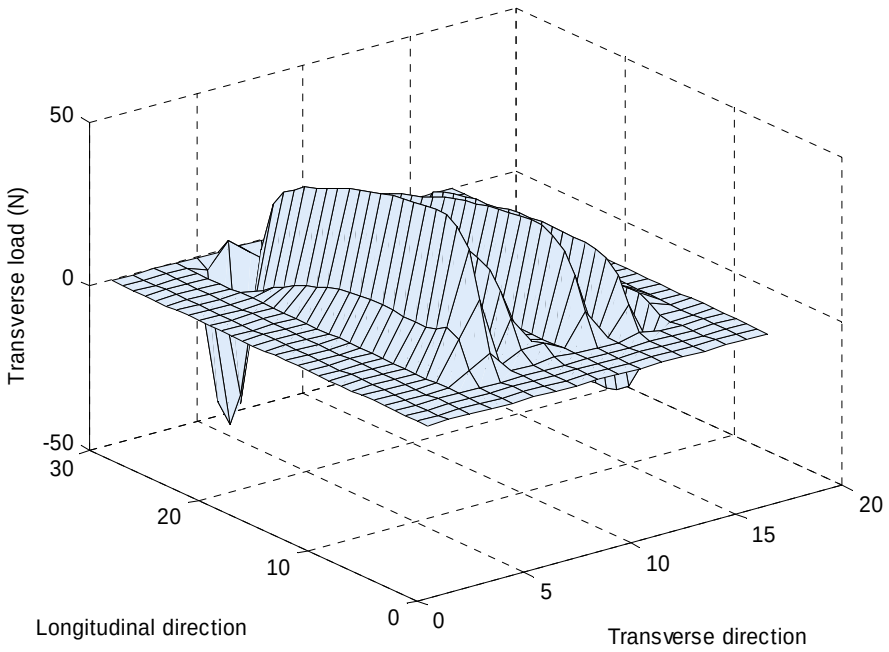

Table 3 Pin signal averaging for test S50550

Outer strip	Mean of pins 12, 13, 21 and 22.
Inner strip	Mean of pins 15, 16, 18 and 19.
Null strip	Mean of pins 14, 17 and 20.

Table 4 Element column assignment for S50550 and S40690

1	2	3	4	5	6	7	8	9
Outer strip	Null strip	Inner strip	Inner strip	Null strip	Inner strip	Inner strip	Null strip	Outer strip

2.2 S40550

Figures 4 to 6 present the measured pin loads for a wheel load of 40kN and a tyre inflation pressure of 550kPa. For S40550, the tyre spanned 9 pins (pins 12–20).

Figure 4 Recorded vertical pin loading on a single tyre with a 40kN wheel load and a tyre inflation pressure of 550kPa

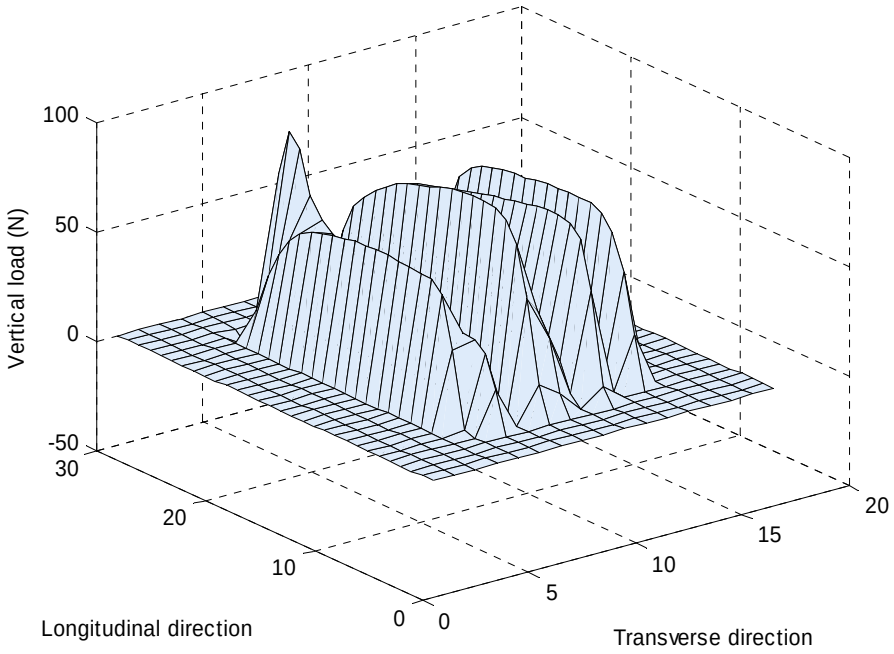

Figure 5 Recorded longitudinal pin loading on a single tyre with a 40kN wheel load and a tyre inflation pressure of 550kPa

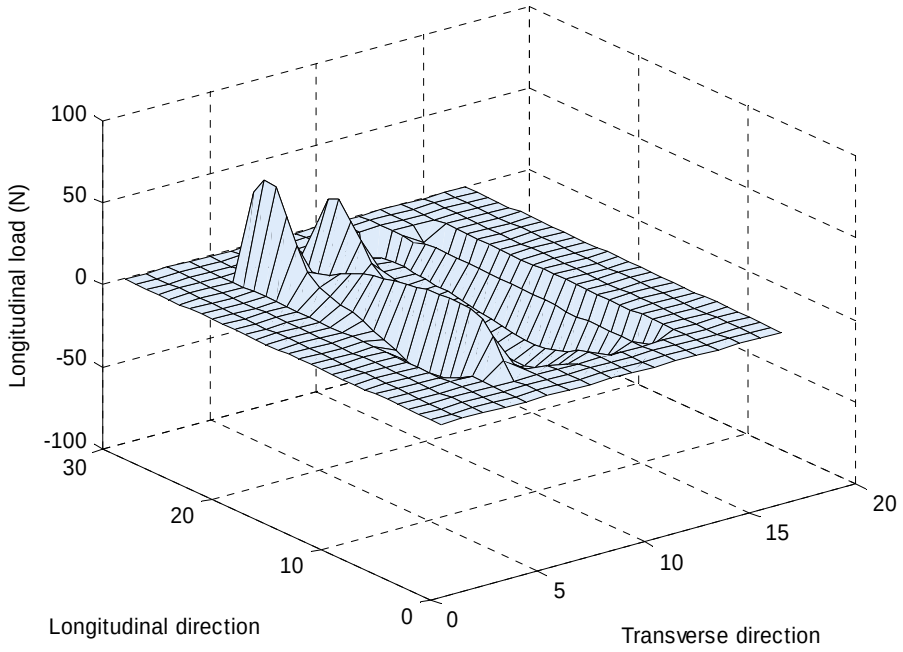

Figure 6 Recorded transverse pin loading on a single tyre with a 40kN wheel load and a tyre inflation pressure of 550kPa

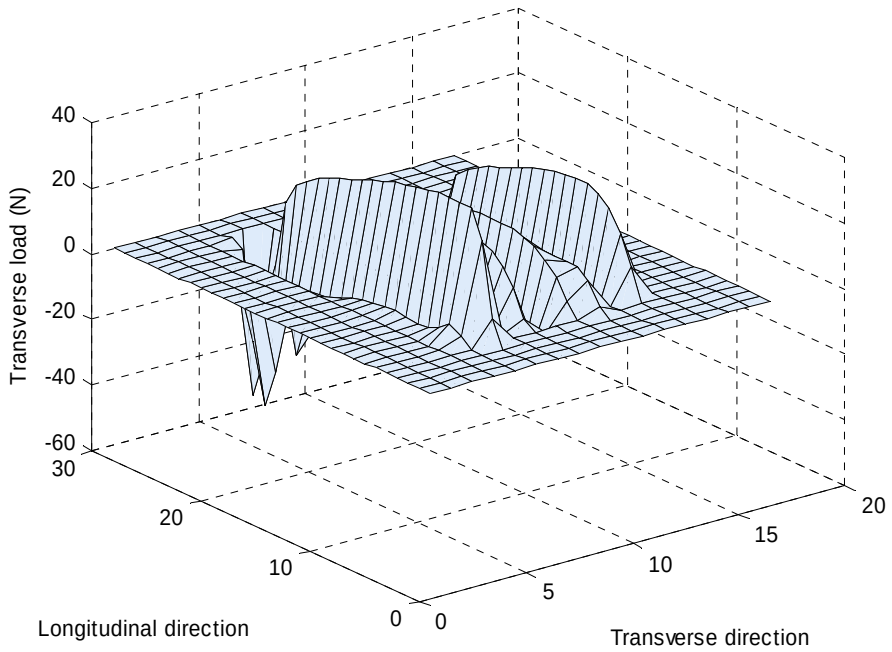

With symmetry assumed in the vertical direction and fixed tyre width, the outer strips were averaged with three pin records as indicated in table 5. Table 6 shows the element assignment.

Table 5 Pin signal averaging for test S40550

Outer strip	Mean of pins 12, 13 and 20
Centre	Mean of 15, 16, 17 and 18
Null	Mean of pins 14 and 19

Table 6 Element column assignment for S40550

1	2	3	4	5	6	7	8	9
Outer strip	Outer strip	Null	Centre	Centre	Centre	Null	Outer strip	Outer strip

2.3 S50690

Figures 7 to 9 show the measured pin loads for a wheel load of 50kN and a tyre inflation pressure of 690kPa.

Figure 7 Recorded vertical pin loading on a single tyre with a 50kN wheel load and a tyre inflation pressure of 690kPa

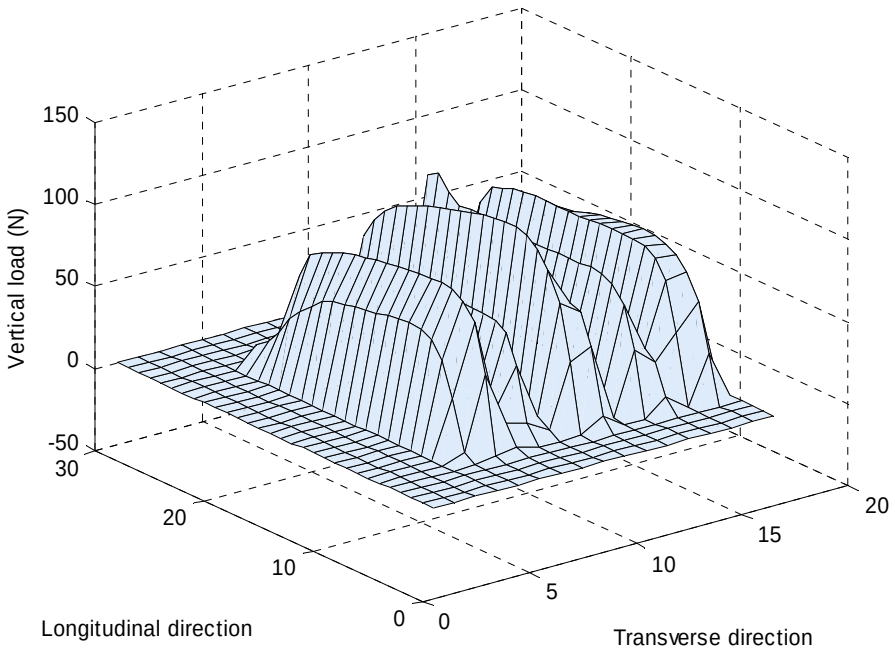

Figure 8 Recorded longitudinal pin loading on a single tyre with a 50kN wheel load and a tyre inflation pressure of 690kPa

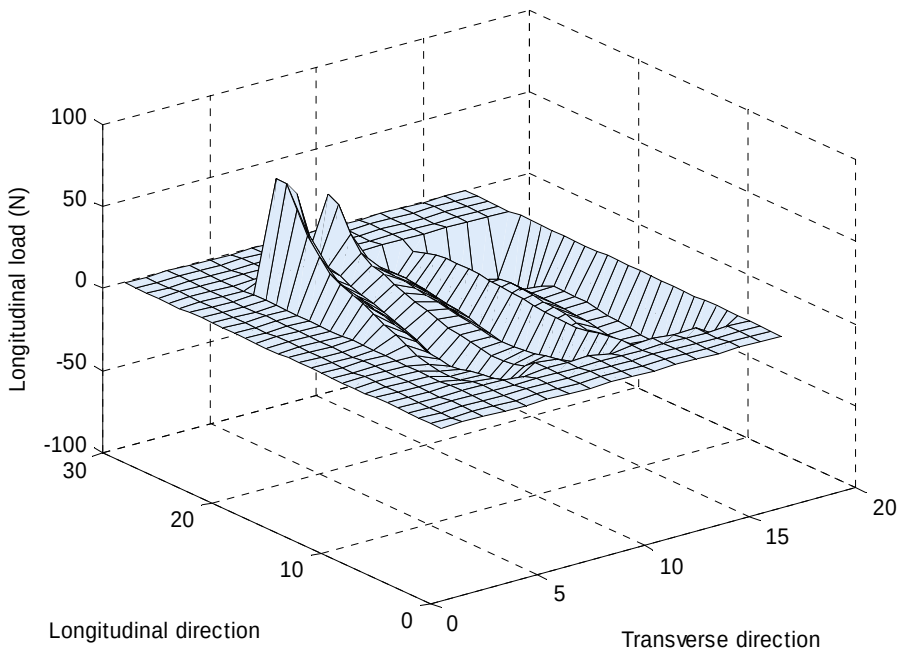

Figure 9 Recorded transverse pin loading on a single tyre with a 50kN wheel load and a tyre inflation pressure of 690kPa

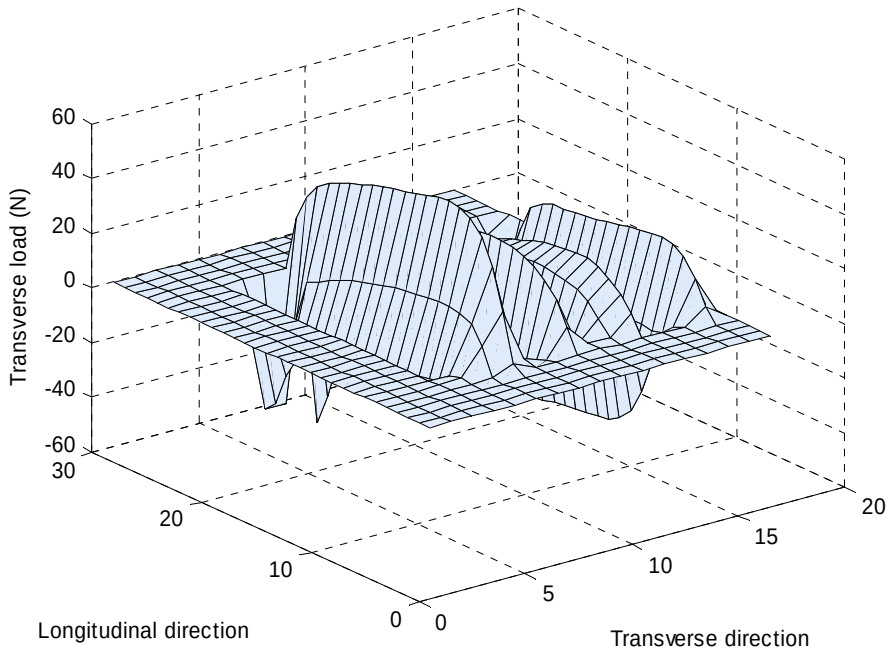

Based on the observed vertical loadings the pin signals were averaged as indicated in table 7 and then nine loading strips were generated as indicated in table 8.

Table 7 Pin signal averaging for test S50690

Outer strip	Mean of pins 11, 12, 21 and 22.
Inner strip	Mean of pins 14 and 19.
Null strip	Mean of pins 13, 15, 18 and 20.
Centre strip	Mean of pins 16 and 17.

Table 8 Element column assignment for S50690

1	2	3	4	5	6	7	8	9
Outer strip	Null strip	Inner strip	Null strip	Centre strip	Null strip	Inner strip	Null strip	Outer strip

2.4 S40690

Figures 10 to 12 show the measured pin loads for a wheel load of 40kN and a tyre inflation pressure of 690kPa. In S40690, the tyre spanned 11 pins (pins 12–22).

Figure 10 Recorded vertical pin loading on a single tyre for a 40kN wheel load and a tyre inflation pressure of 690kPa

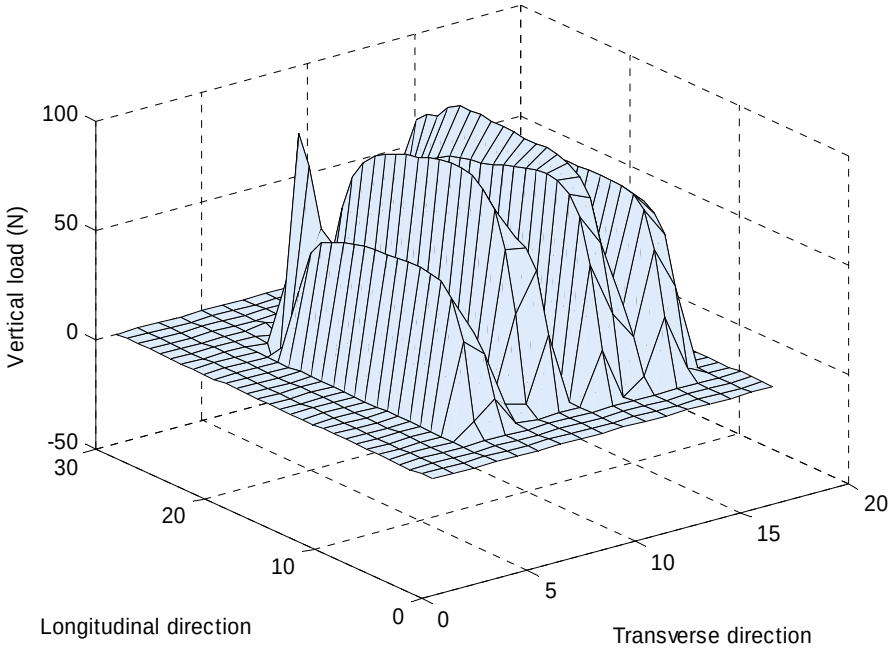

Figure 11 Recorded longitudinal pin loading on a single tyre for a 40kN wheel load and a tyre inflation pressure of 690kPa

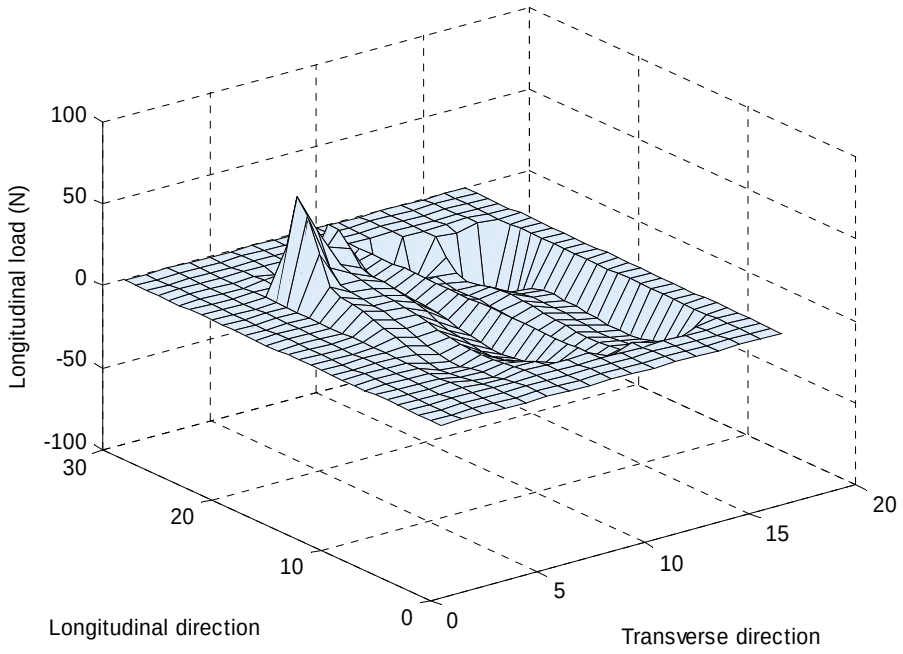

Figure 12 Recorded transverse pin loading on a single tyre for a 40kN wheel load and a tyre inflation pressure of 690kPa

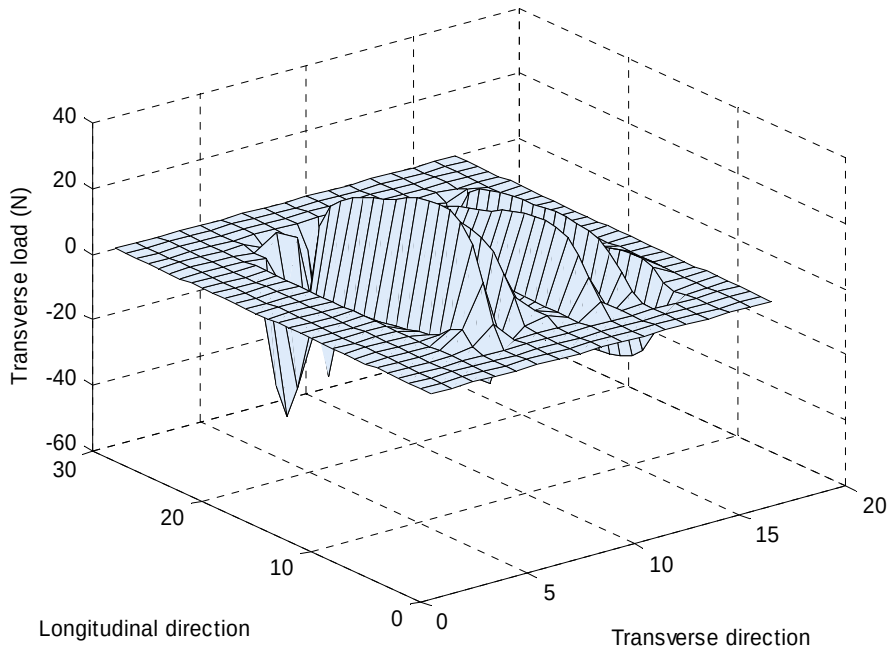

For S40690 the averaging process was as detailed in table 9 and nine loading strips were assigned as indicated in table 10.

Table 9 Pin signal averaging for test S40690

Outer strip	Mean of pins 12, 13, 21 and 22.
Inner strip	Mean of pins 15, 16, 18 and 19.
Null strip	Mean of pins 14, 17 and 20.

Table 10 Element column assignment for S40690

1	2	3		4		5	6	7
Outer strip	Null strip	Inner strip	Inner strip	Null strip	Inner strip	Inner strip	Null strip	Outer strip

2.5 D40280

Figures 13 to 15 show the measured pin loads for a wheel load of 40kN and a tyre inflation pressure of 280kPa.

Figure 13 Recorded vertical pin loading on dual tyres for a 40kN wheel load and a tyre inflation pressure of 280kPa.

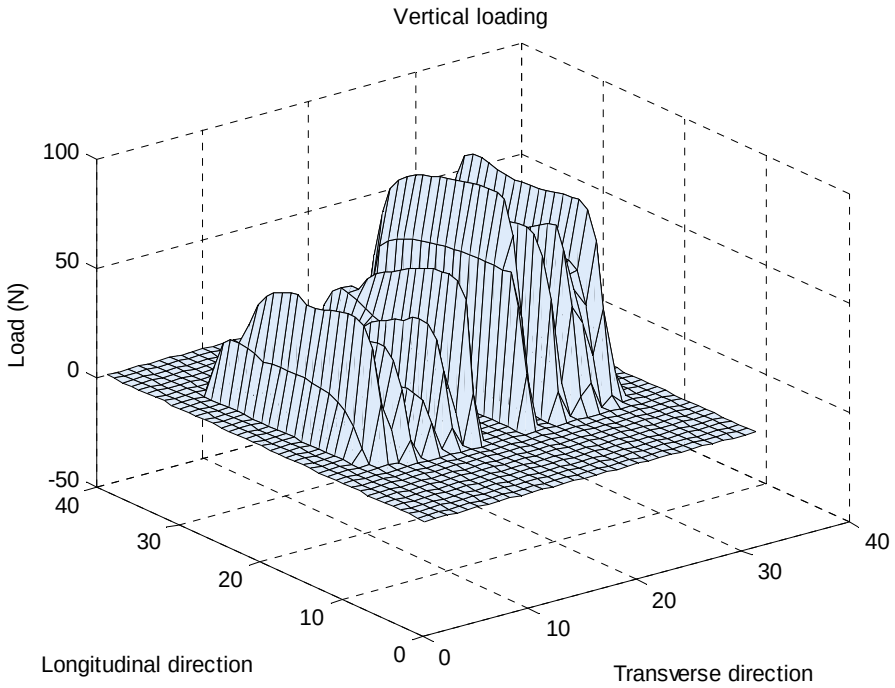

Figure 14 Recorded longitudinal pin loading on dual tyres for a 40kN wheel load and a tyre inflation pressure of 280kPa

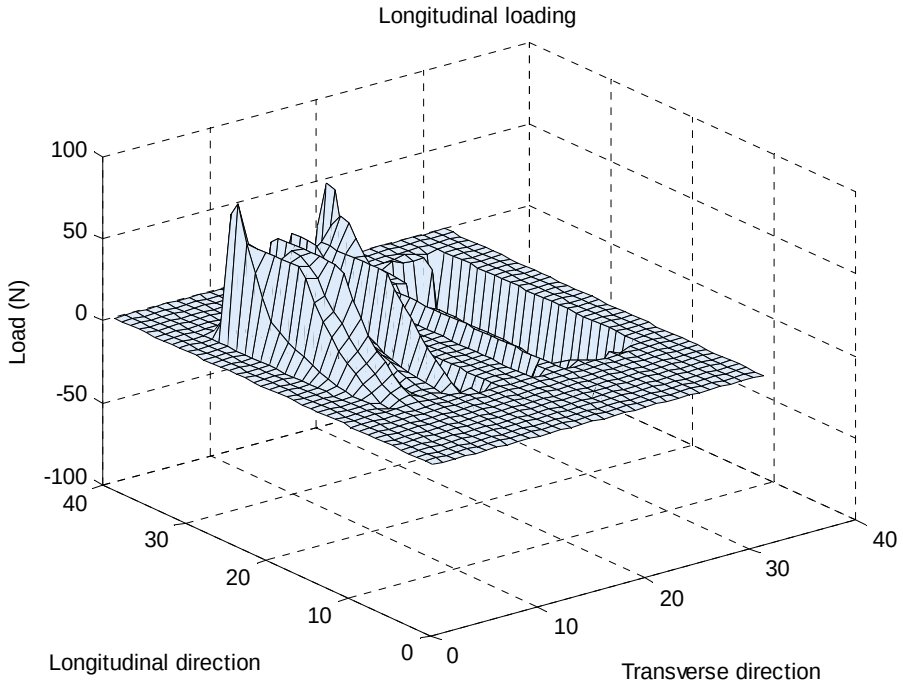

Figure 15 Recorded transverse pin loading on dual tyres for a 40kN wheel load and a tyre inflation pressure of 280kPa

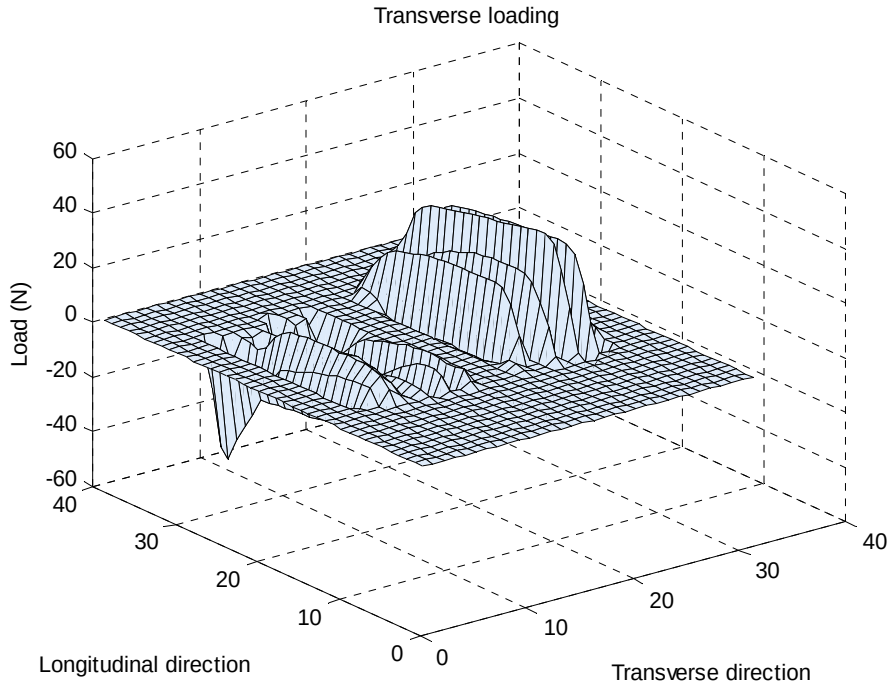

2.6 D40690

Figures 16 to 18 show the measured pin loads for a wheel load of 40kN and a tyre inflation pressure of 690kPa.

Figure 16 Recorded vertical pin loading on dual tyres for a 40kN wheel load and a tyre inflation pressure of 280kPa

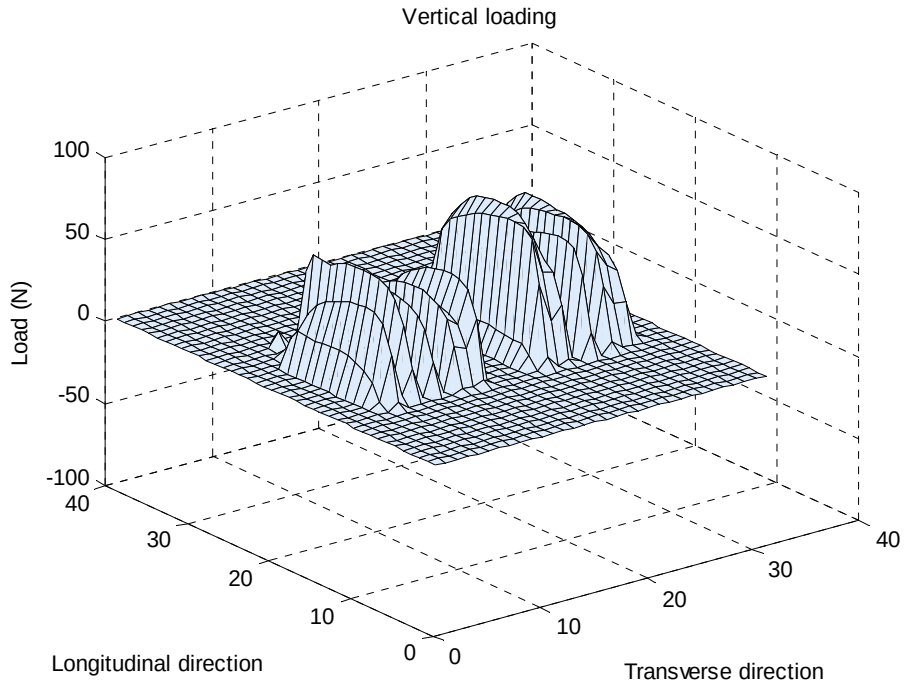

Figure 17 Recorded longitudinal pin loading on dual tyres for a 40kN wheel load and a tyre inflation pressure of 280kPa

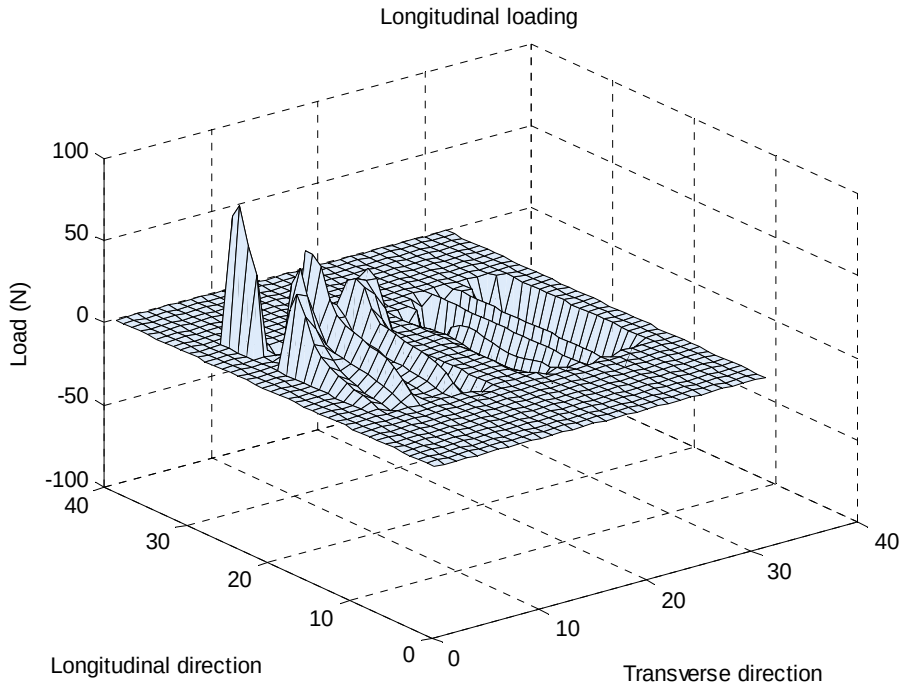

Figure 18 Recorded transverse pin loading on dual tyres for a 40kN wheel load and a tyre inflation pressure of 280kPa

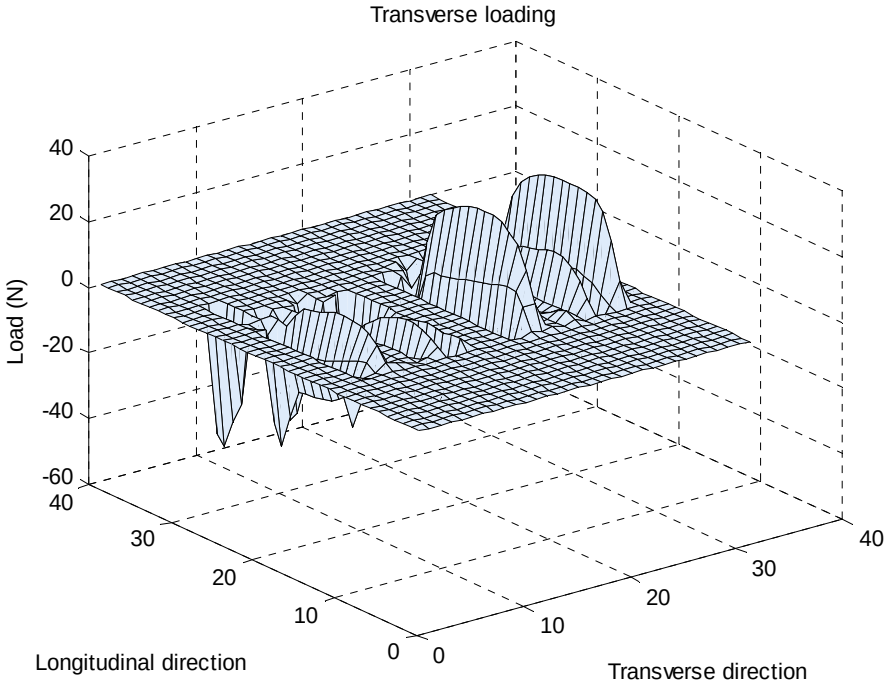

2.7 D50280

Figures 19 to 21 show the measured pin loads for a wheel load of 50kN and a tyre inflation pressure of 280kPa.

Figure 19 Recorded vertical pin loading on dual tyres for a 50kN wheel load and a tyre inflation pressure of 280kPa

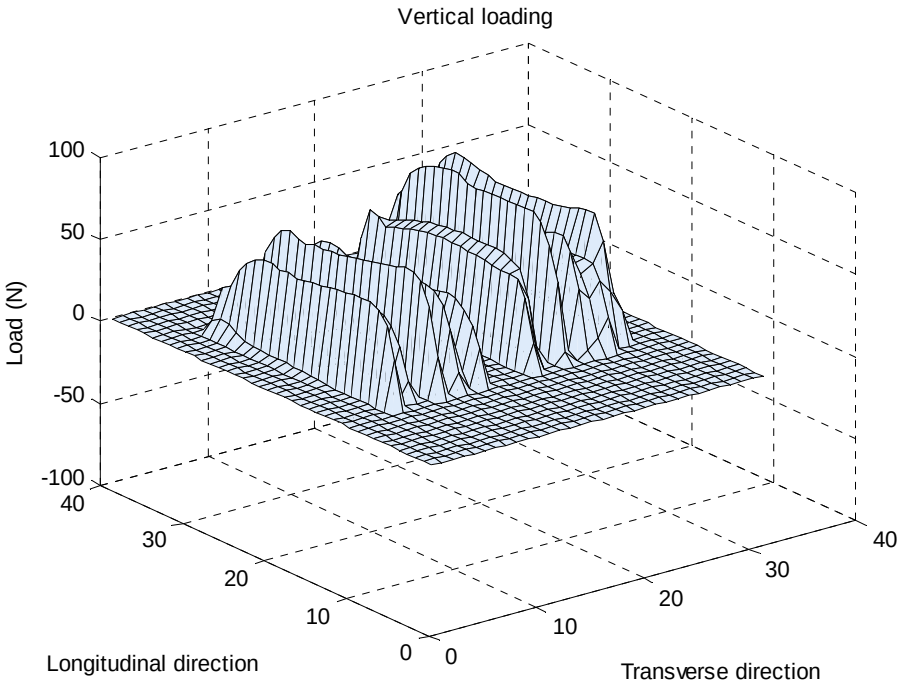

Figure 20 Recorded longitudinal pin loading on dual tyres for a 50kN wheel load and a tyre inflation pressure of 280kPa

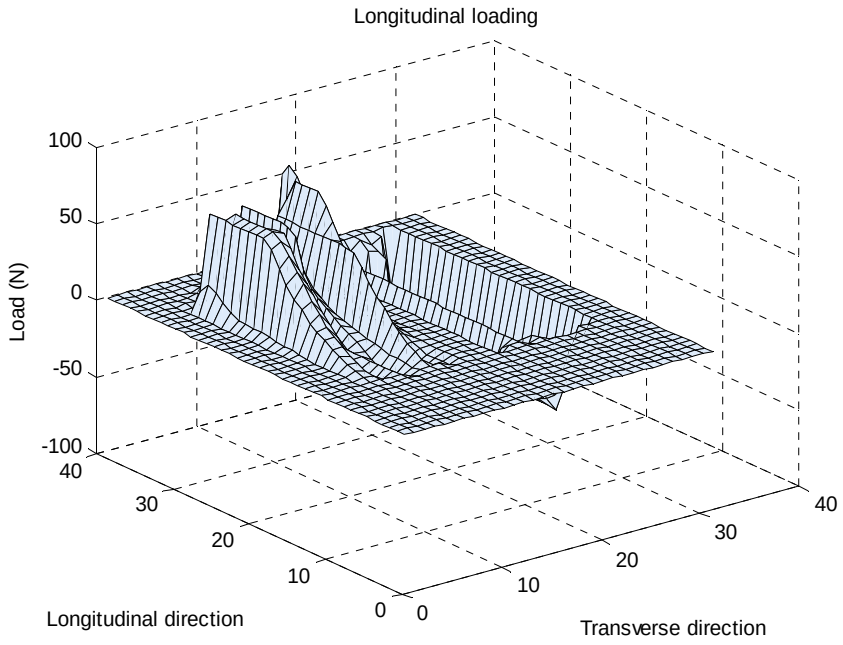

Figure 21 Recorded transverse pin loading on dual tyres for a 50kN wheel load and a tyre inflation pressure of 280kPa.

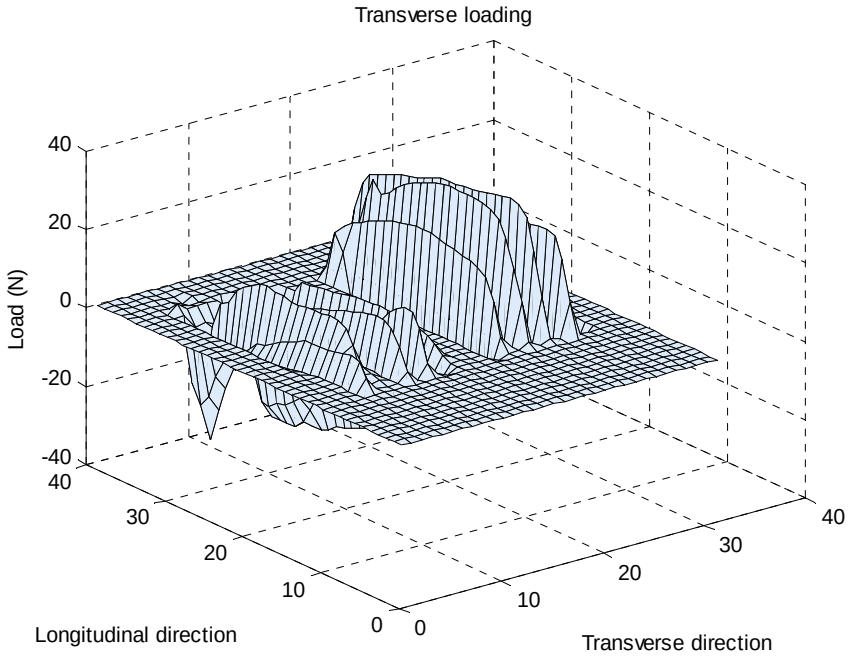

2.8 D50690

Figures 22 to 24 show the measured pin loads for a wheel load of 50kN and a tyre inflation pressure of 690kPa.

Figure 22 Recorded vertical pin loading on dual tyres for a 50kN wheel load and a tyre inflation pressure of 690kPa

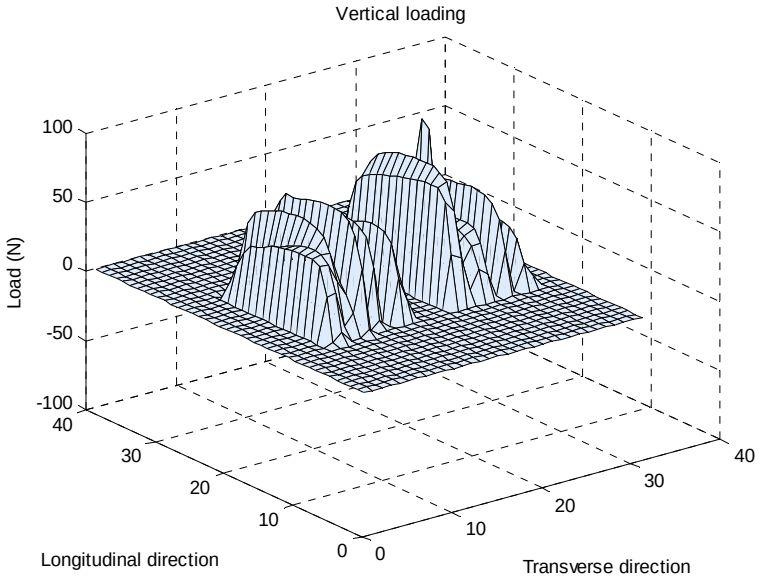

Figure 23 Recorded longitudinal pin loading on dual tyres for a 50kN wheel load and a tyre inflation pressure of 690kPa

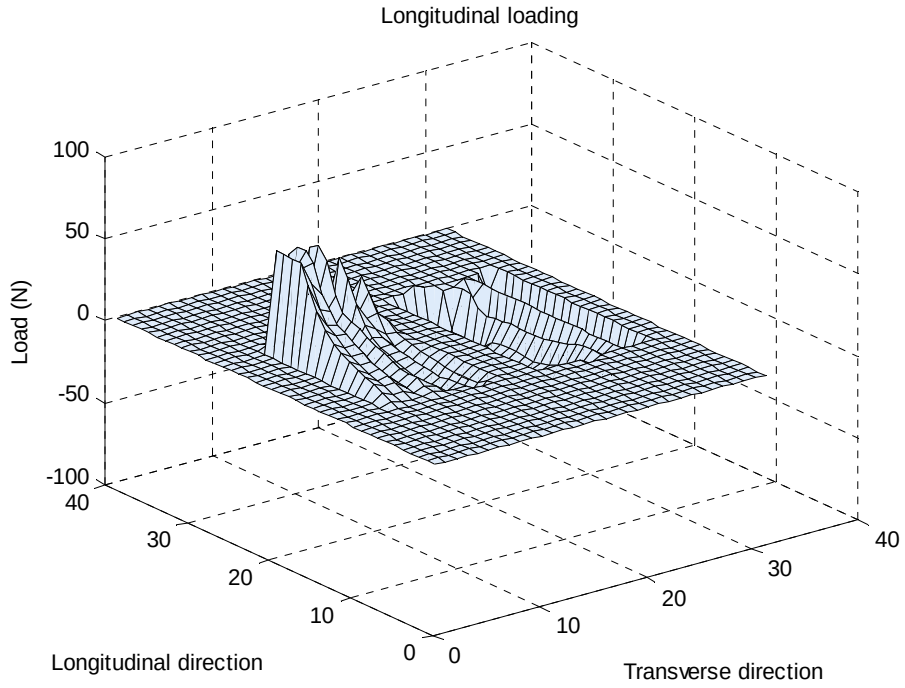

Figure 24 Recorded transverse pin loading on dual tyres for a 50 kN wheel load and a tyre inflation pressure of 690 kPa.

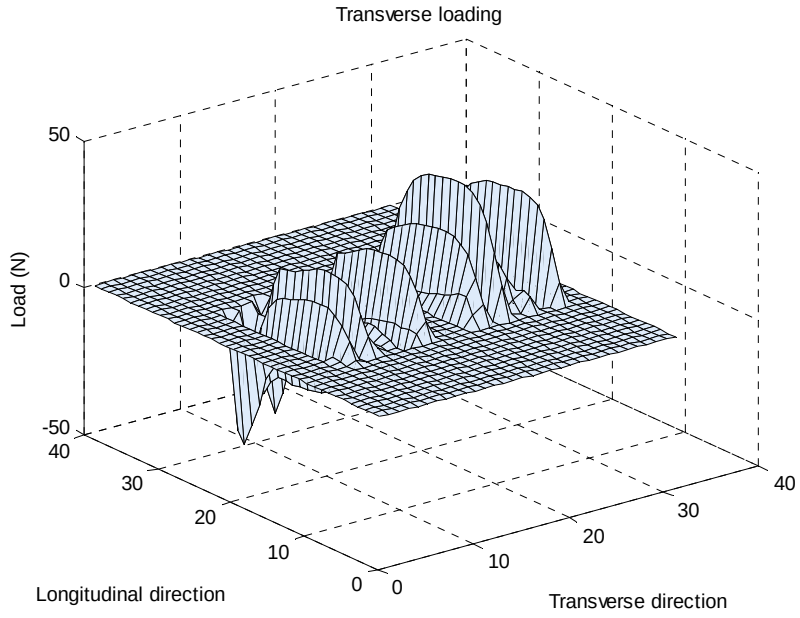

2.9 Record processing

As mentioned earlier, the tyres in each test spanned various numbers of pins. The inferred tyre widths are indicated in table 2. For S40550, table 11 indicates a reduction of width with a decrease in the tyre inflation pressure (when compared to S40690); this does not correspond to the tyre footprints produced at CAPTIF. Consequently, it has been assumed that all tyre widths are 250mm except of S50690 with 275mm (table 2). The area of the tyre footprint is therefore only variable with length which is calculated from the length of the record.

Table 11 Tyre width as a product of pins recording.

	Pins recording a signal	Corresponding tyre width (mm)
S40550	12 to 20	200 ± 50
S40690	12 to 22	250 ± 50
S50550	12 to 22	250 ± 50
S50690	11 to 22	275 ± 50
D40280	1 to 10 and 15 to 24	250/250
D40690	1 to 10 and 15 to 25	250/275
D50280	1 to 11 and 15 to 24	250/250
D50690	2 to 11 and 16 to 25	275/250

For the FE calculations, the single tyre footprint was assigned a width of 9 elements and a length of 6 elements.

Figure 25 demonstrates the vertical load profile along the width of a single tyre loaded with 50kN and having a pressure of 690kPa, this can be compared to the same data plotted in figure 7. The observed profile was used to determine the averaging shown in table 7 and to produce the element loading displayed in table 14.

Figure 25 Vertical pin loading of tyre across the width of the tyre, S50690

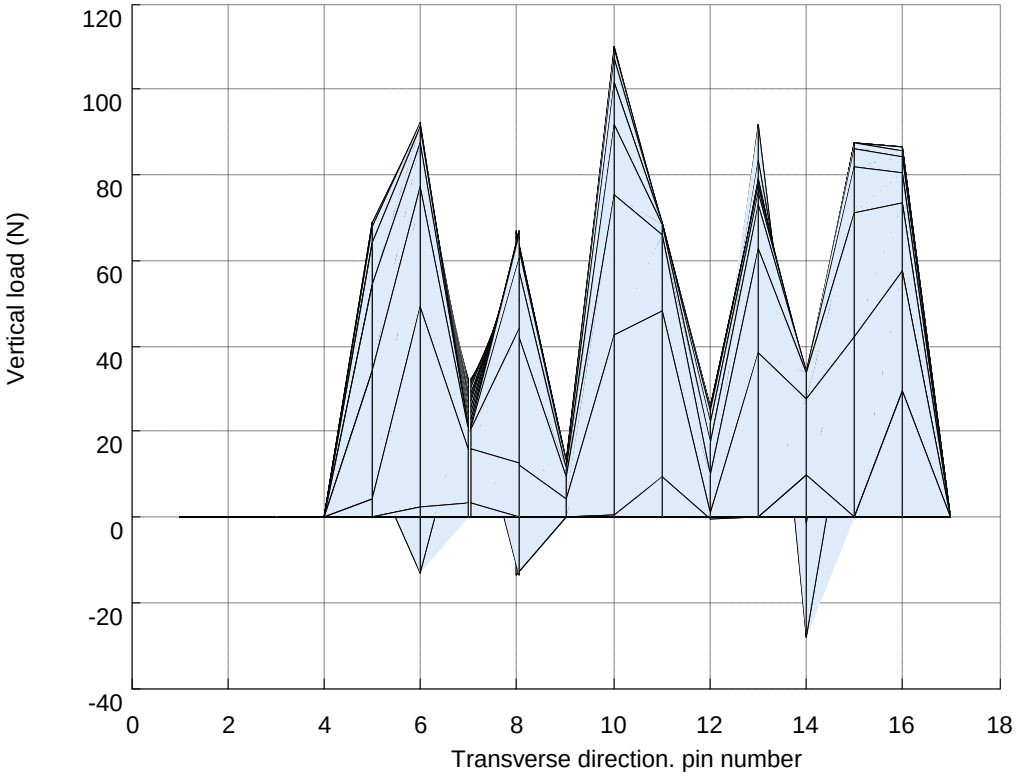

For the FE calculations, the dual tyre footprint was assigned a width of 24 elements (10 elements each wheel and 4 elements the space in-between the wheels) and a length of 6 elements.

Figure 26 shows the vertical load profile along the width of a dual tyre loaded with 50kN and having a pressure of 690kPa. The observed profile was used to produce the element loading displayed in table 14.

Figure 26 Vertical pin loading of tyre across the width of the tyre, D50690

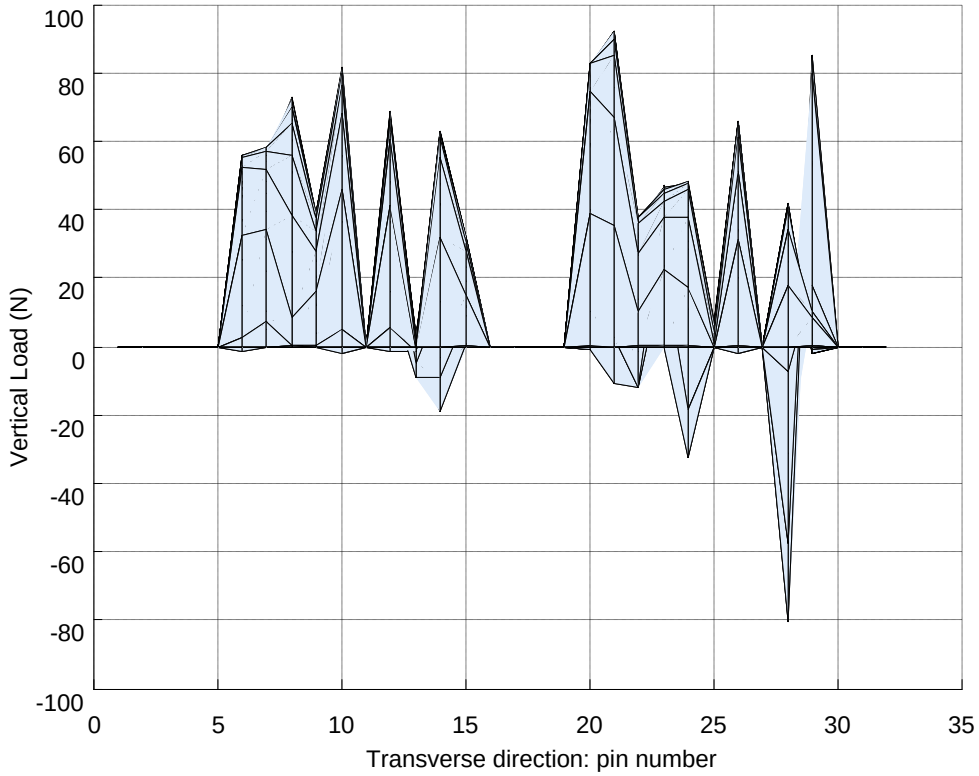

It should however be noted that the results given here are indicative of normally inflated tyres, and hence the higher vertical stresses in the middle of the tyre. In general, higher vertical stresses at the middle of the tyre can be observed for higher tyre inflation pressures. Lower tyre inflation pressures will lead to higher stresses at the edge of the radial tyres.

2.10 Transverse stress values

A similar averaging process was used to assign the transverse stress values for the FE calculations.

2.11 Longitudinal stress values

The asymmetric nature of the longitudinal stress data meant that a different approach was used to determine the longitudinal stress values. A linear variation with width was assumed with the slope being determined from the experimental data.

De Beer (1996) published a paper on the measured vertical, transverse and longitudinal loads generated by a moving free-rolling wheel in a straight line. The report indicated that direct measured vertical loads were about 25% lower than the applied loads by approximately 25%. The resultant transverse and longitudinal load were less than 2% and 3% of the measured vertical load respectively. The method that De Beer has used to calculate these values is relatively unclear; however, at this stage the data from the current study do not support this observation.

The experimental plots reproduced in figures 1 to 12 vary from those presented by De Beer (1996). For the experimental data presented here, there is far more variation in the load across the width of the tyre. This is perhaps to be expected as De Beer performed his experiments on bald tyres in a linear test facility while the CAPTIF tests had ribbed tyres travelling around a circular track.

For stress calculations, an effective load-carrying area was not known. Hence, the loads carried by each pin were integrated over time and then summed to give the total load (resultant vertical force). The total vertical load was assumed to be equal to 40 or 50kN for the corresponding experiments. The measured forces were adjusted so that the resultant vertical force was equal to 40 or 50kN respectively.

3 Finite element model and loading condition

Advances in computing power and experimental characterisation techniques have led to an increased use of the FE method to predict the pavement response under measured tyre/pavement contact stresses. Several researchers (Park et al 2005; Blab 2001; Groenendijk 1998) conducted analysis of the pavement response under measured tyre/pavement contact stresses using FE codes. Among other things, they determined to what extent the non-uniform contact stress distribution should be taken into account and at which depths a simplified contact stress distribution is acceptable.

For a detailed investigation of pavement tyre/pavement contact stresses, a 3D FE model is required. The FE code ReFEM was used to carry out this investigation. Special isoparametric 20-node elements (Bathe 2002) were used that possess 60 degrees of freedom and tri-quadratic displacement shape functions. The modelled tyre/pavement contact stresses were applied as element forces. A rectangular model was developed to simulate a typical New Zealand pavement. Because of the asymmetrical tyre/pavement contact stress distributions measured at CAPTIF, making use of symmetry to reduce the computational effort was not possible. The lengths and the widths of the FE sections were different for each tyre configuration. However, the general pavement structure was consistent for all tyre configurations investigated. Table 12 shows the FE configuration used to model the granular pavement.

Table 12 Details of the pavement investigated

Thickness of the asphalt layer [mm]	Number of the elements in vertical direction of the asphalt [-]	Thickness of the base course [mm]	Number of the elements in vertical direction of the base course [-]	Thickness of the subgrade [mm]	Number of the elements in vertical direction of the subgrade [-]
40	2	300	4 (single tyre) 3 (dual tyre)	1000	2 (single tyre) 3 (dual tyre)

Figure 27 presents the FE mesh dimensions modelled for the single and dual tyres.

Table 13 FE Mesh dimensions.

	Mesh width [mm]	Mesh length (mm)
S40550	1,596	1,980
S40690	1,596	1,872
S50550	1,596	2,160
S50690	1,738	1,836
D40280	1,575	1,857
D40690	1,575	1,400
D50280	1,575	2,024
D50690	1,575	1,515

As shown in figure 27 the mesh used in the analysis was finest at the tyre/pavement contact area in order to take the measured tyre/pavement contact stress distribution into account as accurate as possible. The bottom of the subgrade was prevented from movement in the three coordinate directions, but the sides of the model were completely unrestrained. Generally, the FE mesh was constructed relative to a right-handed Cartesian coordinate system as follows:

The X, or 1, coordinate is the transverse or lateral direction.

The Y, or 2, coordinate is the longitudinal or moving wheel direction.

The Z, or 3, coordinate is the vertical direction and the plane Z = 0 is located at the bottom of the subgrade layer.

Figure 27 FE mesh – single tyre

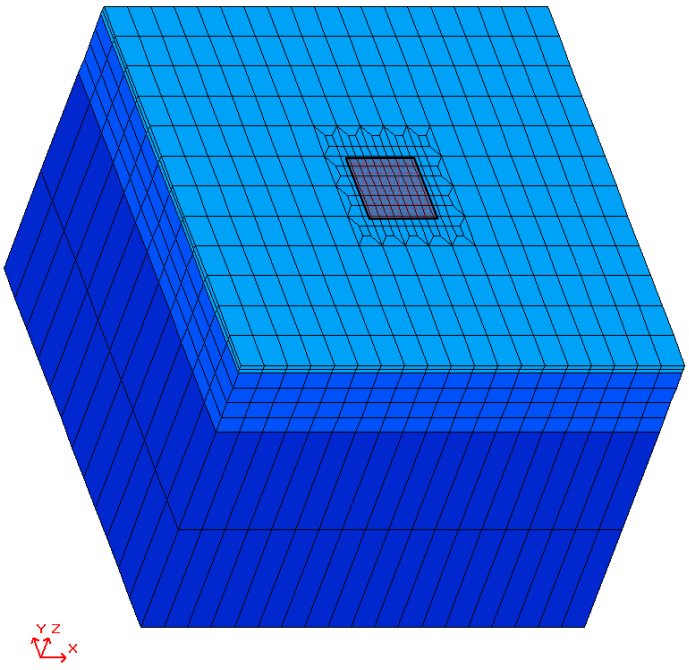

3.1 Uniformly distributed tyre/pavement contact stress

Firstly, FE element calculations were conducted assuming a uniformly distributed stress over the tyre/pavement contact area. In order to reflect the calculated contact areas determined in the testing stage of this research, the modelled contact stress shown in table 14 were used.

Table 14 Tyre dimensions and tyre/pavement contact stresses used for the FE calculation

Tyre	Tyre widths [mm]	Tyre lengths [mm]	Contact stress [kPa]
S40550	250	330	480
S40690	250	310	510
S50550	250	360	550
S50690	275	310	590
D40280	250/250	370	220
D40690	250/275	280	290
D50280	250/250	410	250
D50690	275/250	300	300

Figures 28 and 29 illustrate the loading areas for single and dual tyres in red.

Figure 28 Loaded area, single tyre

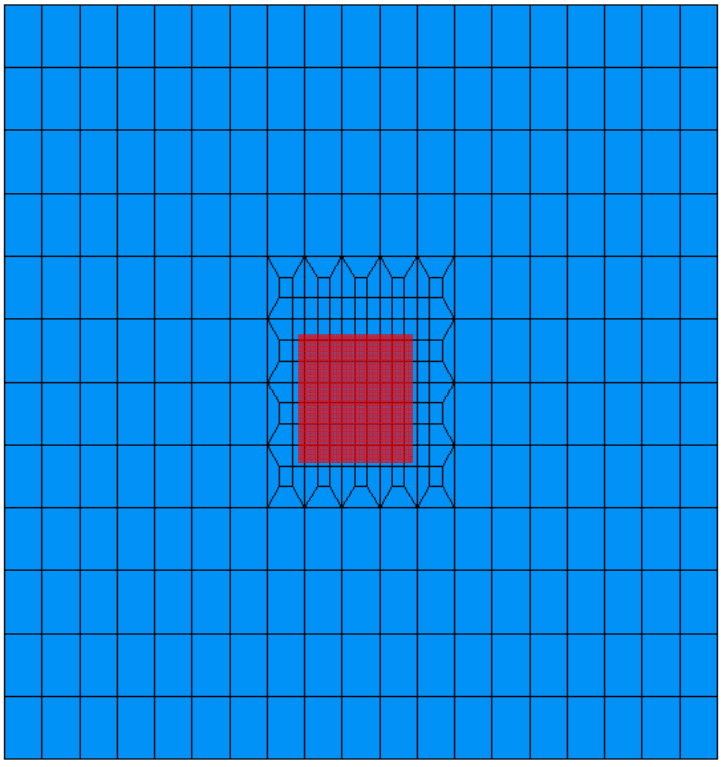

Figure 29 Loaded area, dual tyres

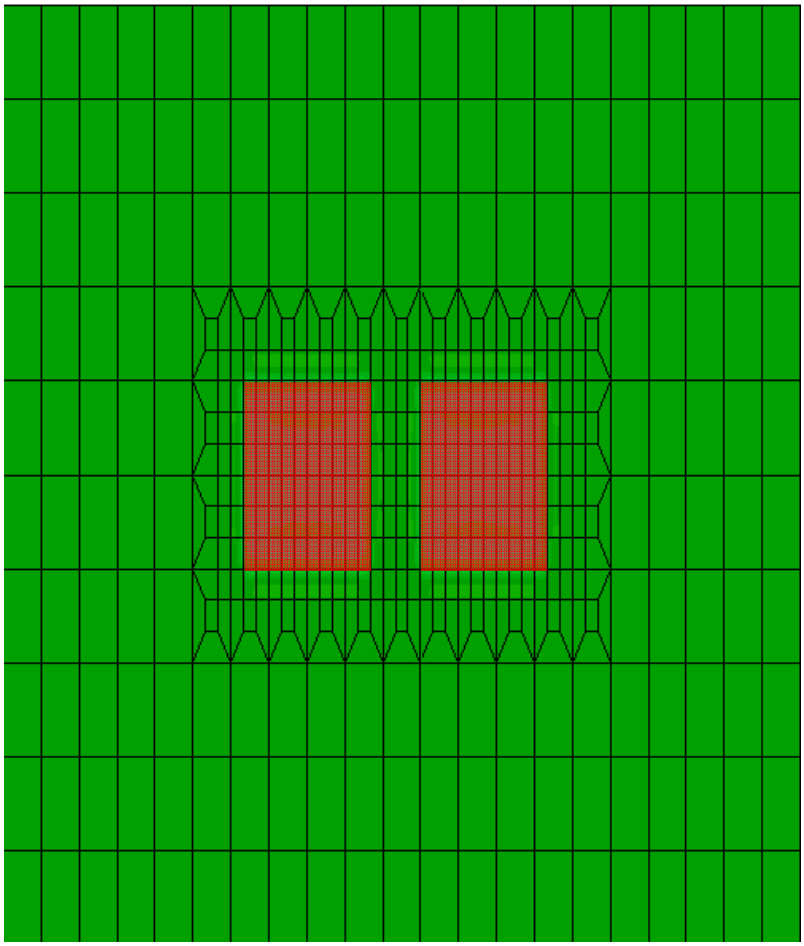

3.2 Non-uniformly distributed tyre/pavement contact stress

Typical results after FE calculation input stress patterns are illustrated in figures 30, 31 and 32 for S40690.

Figure 30 Vertical modelled stress for S40690 after processing of load data

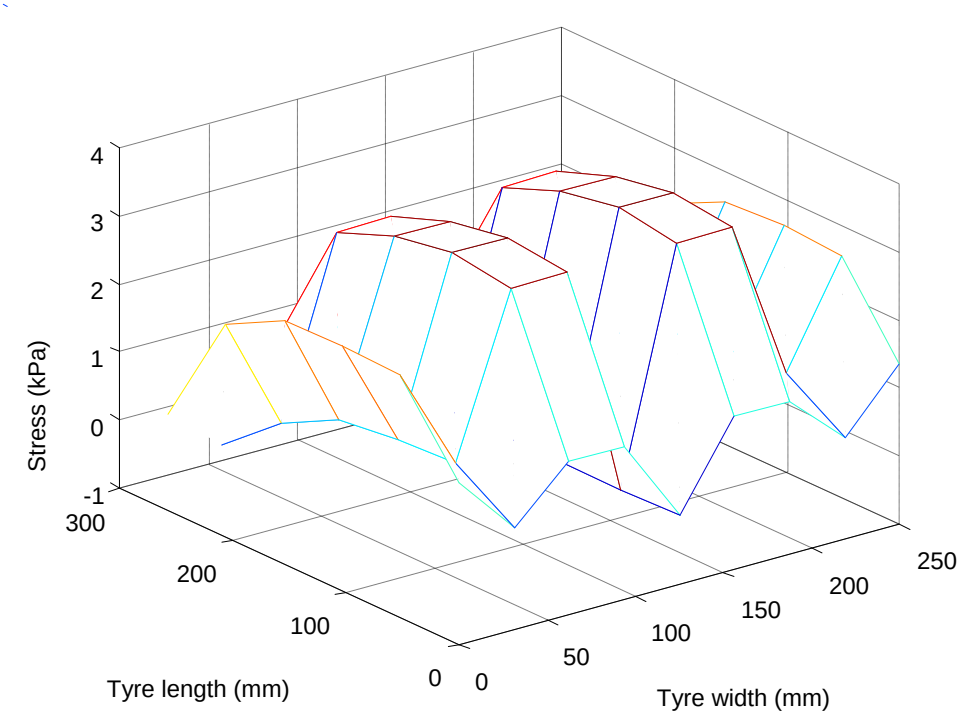

Figure 31 Transverse modelled stress for S50690 after processing of load data

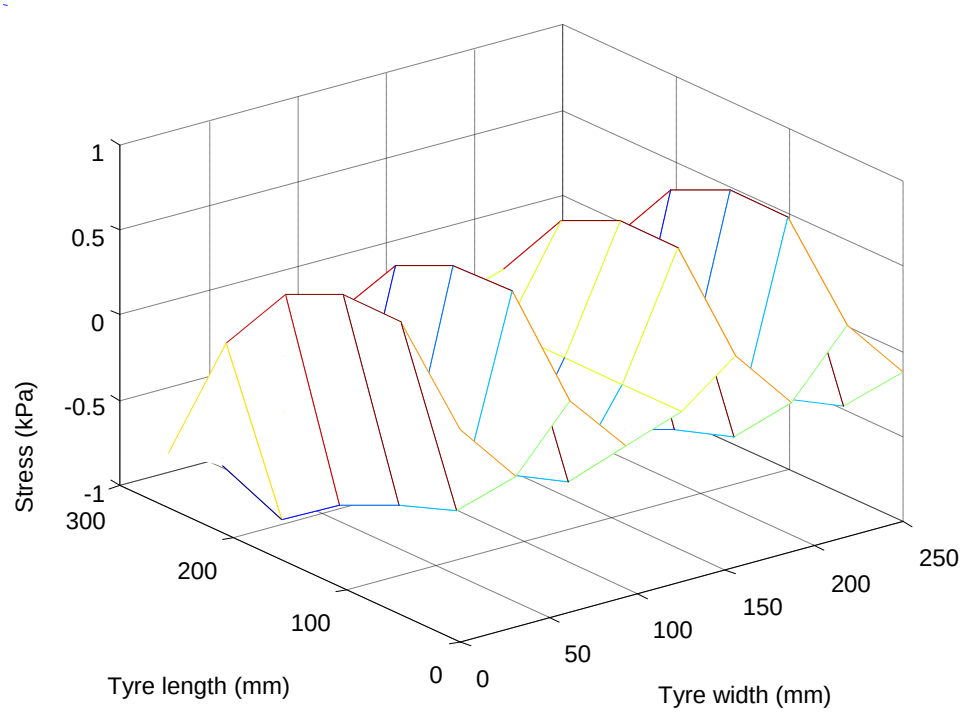

Figure 32 Longitudinal modelled stress for S40690 after processing of the load data

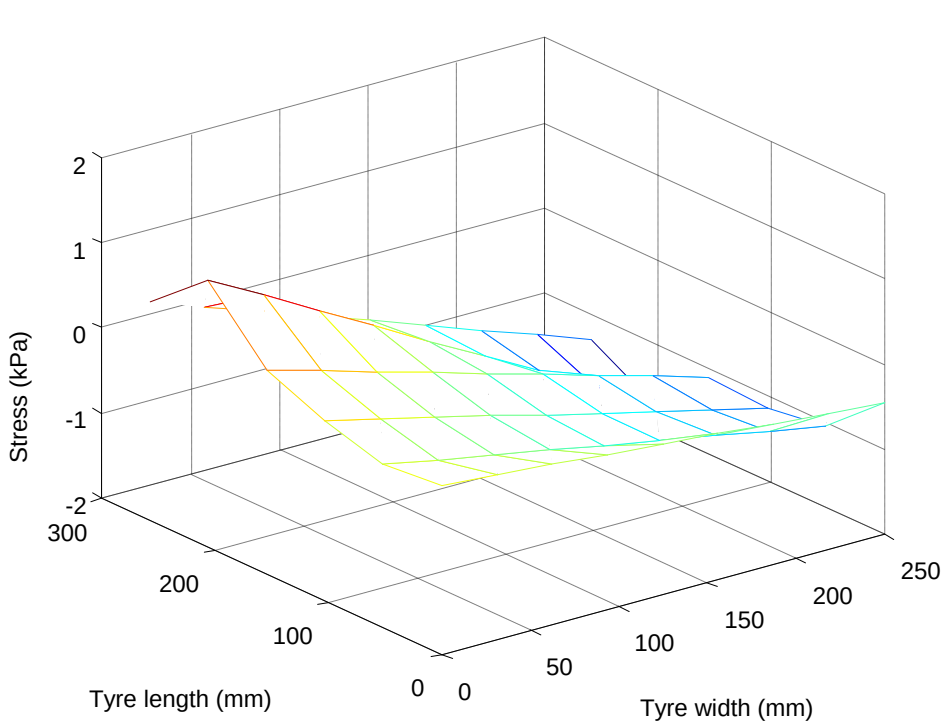

Tables 15 and 16 display the element numbers of the loaded area for the single/dual tyre for the FE calculations.

Table 15 Element numbers related to the loaded area – single tyre

	Transverse								
Longitudinal	1	7	13	19	25	31	37	43	49
	2	8	14	20	26	32	38	44	50
	3	9	15	21	27	33	39	45	51
	4	10	16	22	28	34	40	46	52
	5	11	17	23	29	35	41	47	53
	6	12	18	24	30	36	42	48	54

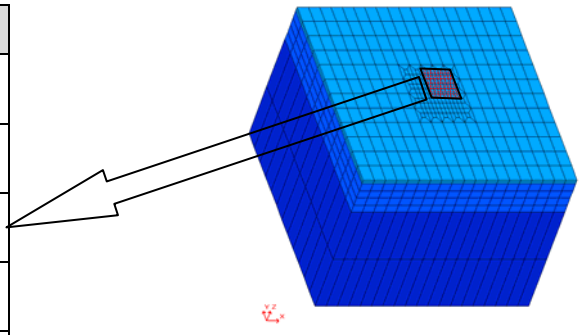

Table 16 Element numbers relating to the loaded area – dual tyre

	Transverse																								
Longitudinal	6	12	18	24	30	36	42	48	54	60	66	72	78	84	90	96	102	108	114	120	126	132	138	144	150
	5	11	17	23	29	35	41	47	53	59	65	71	77	83	89	95	101	107	113	119	125	131	137	143	149
	4	10	16	22	28	34	40	46	52	58	64	70	76	82	88	94	100	106	112	118	124	130	136	142	148
	3	9	15	21	27	33	39	45	51	57	63	69	75	81	87	93	99	105	111	117	123	129	135	141	147
	2	8	14	20	26	32	38	44	50	56	62	68	74	80	86	92	98	104	110	116	122	128	134	140	146
	1	7	13	19	25	31	37	43	49	55	61	67	73	79	85	91	97	103	109	115	121	127	133	139	145

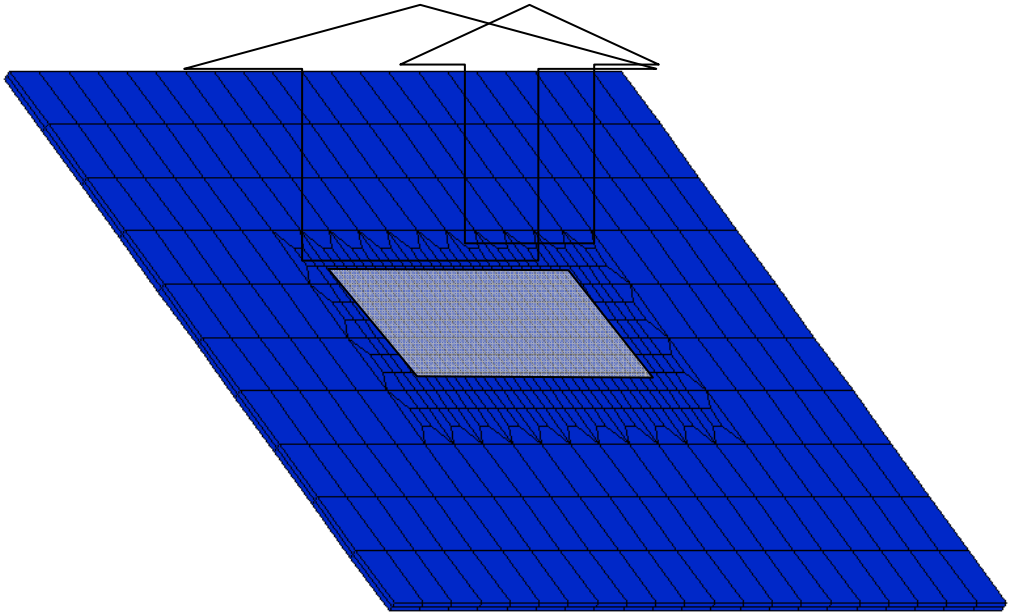

3.3 Material models

3.3.1 Asphalt

The asphalt layer was treated as linearly elastic (ν = 0.35). An E-value of 3,000 N/mm² was assumed.

3.3.2 Base course

In order to determine the parameter for the elastic and plastic model, repeated load triaxial tests (RLT) tests were conducted on a typical New Zealand base course material (Pounds Road Greywacke) that was used at CAPTIF for experiments. Resilient modulus tests as well as plastic strain tests according to the draft of the TNZ RLT Standard (TNZ 2007) were conducted at a degree of compaction (DOC) (95%) and at 70% of the optimum moisture content (OMC).

Nonlinear Dresden Model for UGM

On the basis of RLT testing an empirical non-linear elastic-plastic deformation design model (Dresden Model) was formulated for the base course material. This model was implemented in the FE program ReFEM. In this section only a short overview on the modelling of the UGM is given. Further details are

available elsewhere (Oeser 2004; Werkmeister 2003; Gleitz 1996). This non-linear elastic model is expressed in terms of modulus of elasticity E and Poisson's ratio ν as follows:

$$E = p_a \left(Q + C \cdot \left(\frac{\sigma_3}{p_a} \right)^{Q_1} \right) \cdot \left(\frac{\sigma_1}{p_a} \right)^{Q_2} + D \quad (1)$$

$$\nu = R \cdot \frac{\sigma_1}{\sigma_3} + A \cdot \frac{\sigma_1}{p_a} + B \quad (2)$$

where σ_3 [kPa] is the minor principal stress (absolute value); σ_1 [kPa] is the major principal stress (absolute value); D [kPa] is the constant term of modulus of elasticity; Q, C, Q_1, Q_2, R, A, B are model parameters and p_a is the atmospheric pressure [kPa]. On the basis of the multi-stage RLT tests documented in Arnold (2004) it is possible to determine the parameters of the elastic model.

The model includes a stress-dependent stiffness dependent upon the residual in-situ confining stress. The residual stress has the effect of reducing the strains at small stress levels. The parameter D is mainly influenced by macroscopic parameters like the degree of compaction of the UGM, fines content, grain shape, and water content. The RLT results do not allow determination of the parameter D because the residual stress needs some time to develop in a real pavement construction. Using the CAPTIF results it was possible to determine the value of stress-dependent stiffness for the materials investigated. Table 17 shows the parameters for the Dresden Model used for the FE calculation process.

Table 17 Parameters for the elastic Dresden-Model

Material		**Pounds Road greywacke**
Elastic Dresden-Model		DoC 97%
Q	[-]	14,004
C	[-]	6,540
Q1	[-]	0.346
Q2	[-]	0.333
D	[kPa]	65,000
R	[-]	0.056
A	[-]	-0.0006
B	[-]	0.483
p_a	[kPa]	1

3.3.3 Subgrade

The subgrade was modelled as a linearly elastic material with an E-value of 70 N/mm² and a ν-value of 0.4.

4 Results of analysis

4.1 Introduction

One aim of the research was to compare the results of pavement response and behaviour models when the inputs were the measured non-uniform tyre/pavement contact stresses and an assumed uniform tyre/pavement contact stress. The FE program ReFEM was used to determine the effect of the more accurate contact stress distribution on the response and the rutting performance of pavements.

Because in thin pavements the unbound granular base layer plays the most important role for the pavement response, the research was focused on the stress and strain distribution in the base course. The authors are aware that modelling a uniform vertical tyre/pavement contact stress compared to non-uniform tyre/pavement contact stress distribution has a significant effect on the calculated stress and strain distribution within the asphalt layer as well. However, this effect will be not investigated in this report.

When analysing the results of the FE calculations it should be kept in mind that the measurements of the tyre/pavement contact stress distribution in this research were conducted on powered tyres. In addition, the tyres were constantly driving around a 9m radius bend. Compared to free rolling tyres that are travelling in a straight line, this will have a significant effect on the tyre/pavement contact stress distribution. The tyre alignment and the camber will also influence the tyre/pavement contact stress distribution. For these reasons, the tyre/pavement contact stress distributions measured within this project at the CAPTIF facility are different compared to these tyre/pavement contact stress distributions measured elsewhere (eg by De Beer (1986) under a free rolling wheel.

In the following sections, the results of the FE calculations in terms of the vertical elastic stresses, vertical elastic strains, elastic surface deflections, shear stresses and shear strains are analysed.

4.2 Vertical stress distribution

One of the most important elements in pavement design is the stress distribution. The non-uniformity of the measured vertical contact stress distribution is due partly to the bending stiffness of the tyre carcass.

Figure 33 illustrates the pattern of vertical compressive stress developed in the pavement structure for both a uniform and the modelled non-uniform tyre/pavement contact stress distribution when a 40kN loaded single wheel with a tyre inflation pressure of 690kPa travels over the pavement surface. The patterns show that the non-uniform tyre /pavement contact stresses result in more concentrated stress distributions in the asphalt layer and the top of the base course when compared with the results obtained from uniform vertical stresses. Clearly identifiable are the effects from the ribs of the tyre.

Figure 33 Vertical pavement stresses under a 40 kN tyre load and tyre inflation pressure of 690 kPa – uniform vertical contact pressure (left) and modelled vertical, transverse, and longitudinal contact stresses (right)

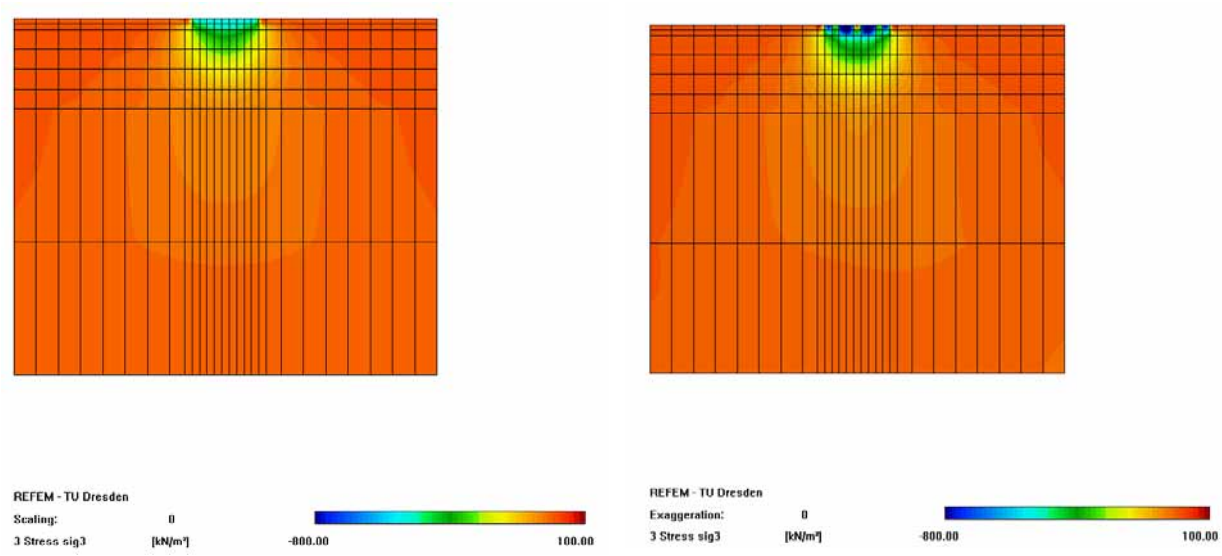

For the experiments S40550 and S50690 the modelled non-uniform tyre/pavement contact stress distributions have a peak in the centre of the tyre. Consequently, the greatest vertical stress in the base course will occur below the centre of the tyre. This is not the case for S40690 and S50550 which have a low stress values in the centre.

Figure 34 illustrates the pattern of vertical compressive stress developed in the pavement structure for both a uniform and a modelled non-uniform tyre/pavement contact stress distribution when a 40kN loaded dual wheel with a tyre inflation pressure of 690 kPa travels over the pavement surface. As already observed for the single tyres, the patterns show that the modelled non-uniform tyre/pavement contact stresses result in more concentrated stress distributions in the asphalt layer and the top of the base course when compared with the results obtained from uniform vertical stresses. Furthermore, it can be seen clearly that for the modelled contact pressure at CAPTIF the inner wheel is loaded significantly more than the outer wheel.

Figure 34 Vertical pavement stresses under a 40 kN dual tyre load with tyre inflation pressure of 690 kPa – uniform vertical contact pressure (left) and modelled vertical, transverse, and longitudinal contact stresses (right)

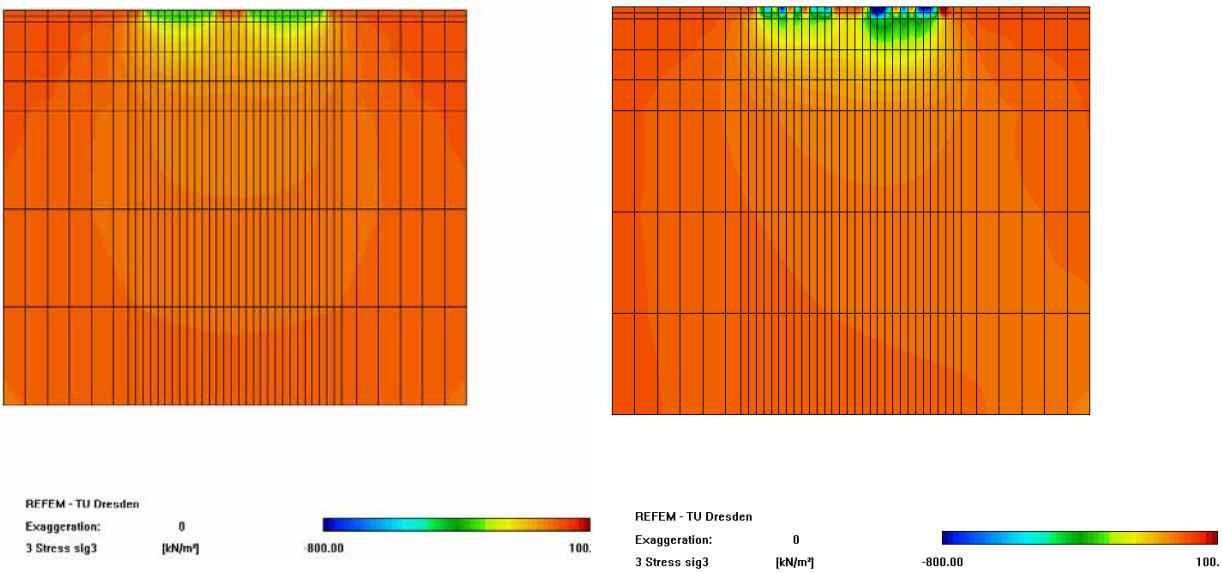

Figures 35 and 36 show the development of the vertical pavement stresses under the tyres for the different load configurations and tyre inflation pressures. It can be seen that the uniform and non-uniform tyre/pavement contact stress distribution cause different vertical stress distributions in the pavement. For the modelled non-uniform tyre/pavement contact stresses applied a higher vertical stresses in the base course can be observed compared to the uniform contact stresses. Furthermore, the rib position will significantly influence the stresses within the thin asphalt layer as evidenced by S40690 and S50550. The results from the FE analysis showed that the contact pressure distributions highly influence the vertical stresses within the top 200mm. At greater depths the differences in the vertical stress values between the two approaches become insignificant (figure 37). The rib position will significantly influence the stress distribution in the asphalt layer: the low magnitudes in vertical stress in the asphalt layer for the S40690 and S50550 occur due to the gap between the ribs at the centre of the wheel (figure 37). At CAPTIF the inner wheel was loaded more heavily compared to the outer wheel for the dual tyres. At greater depths the differences in the vertical stress values between the two approaches (uniform and non-uniform tyre/pavement contact stress distribution) are visible for the dual tyres (figure 38).

Figure 35 Vertical stress at the centre of the tire contact area versus pavement depths – single wheel

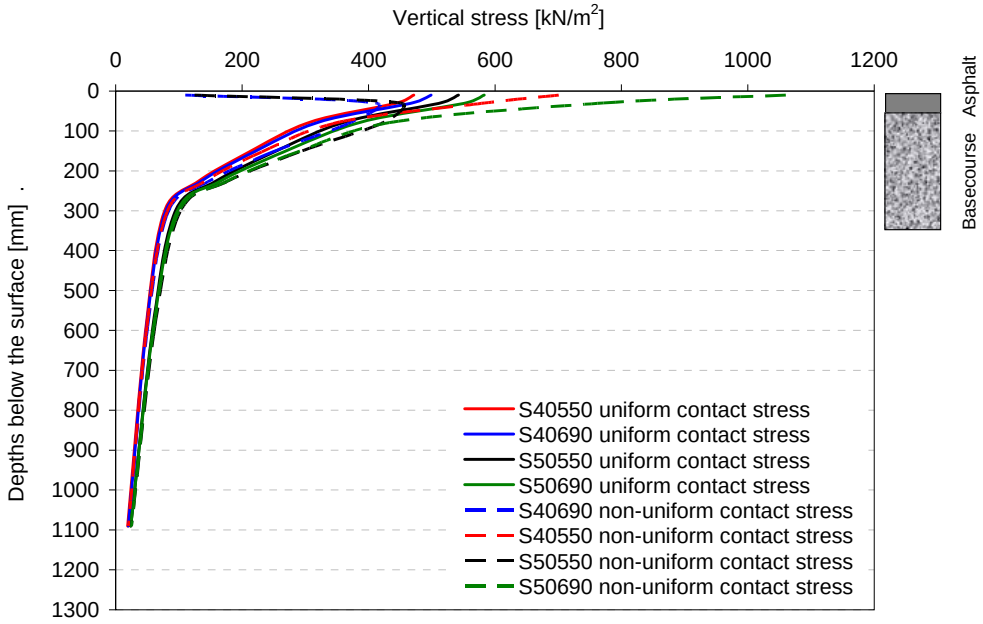

Figure 36 Vertical stress at the centre of the tire contact area (inner wheel) versus pavement depths – dual tyre

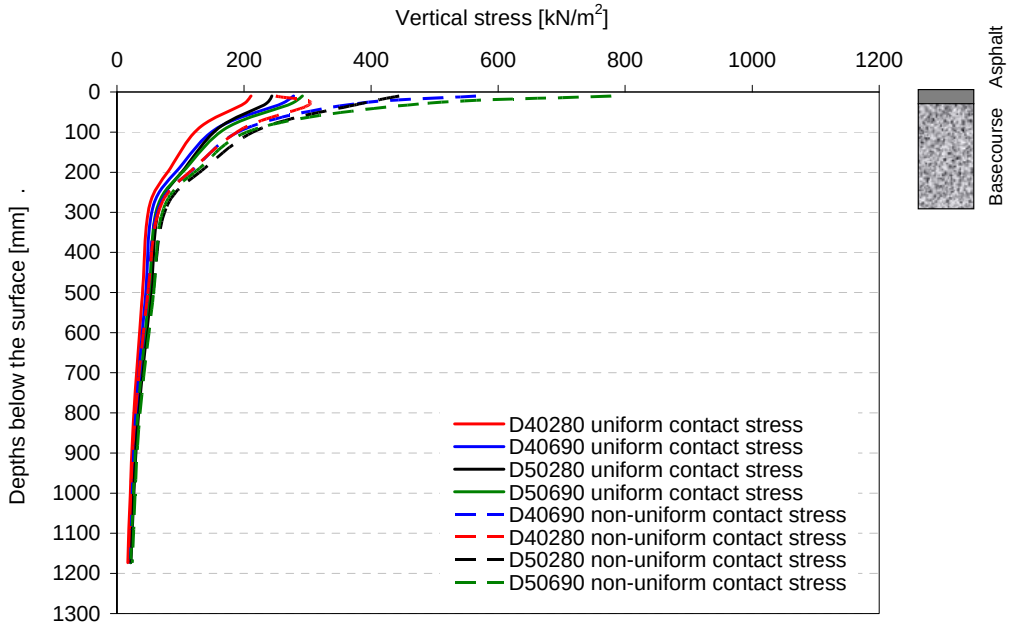

Figure 37 Ratio between vertical stresses at the centre of the tire contact area versus pavement depths (asphalt layer magnitudes are not displayed) – single wheel

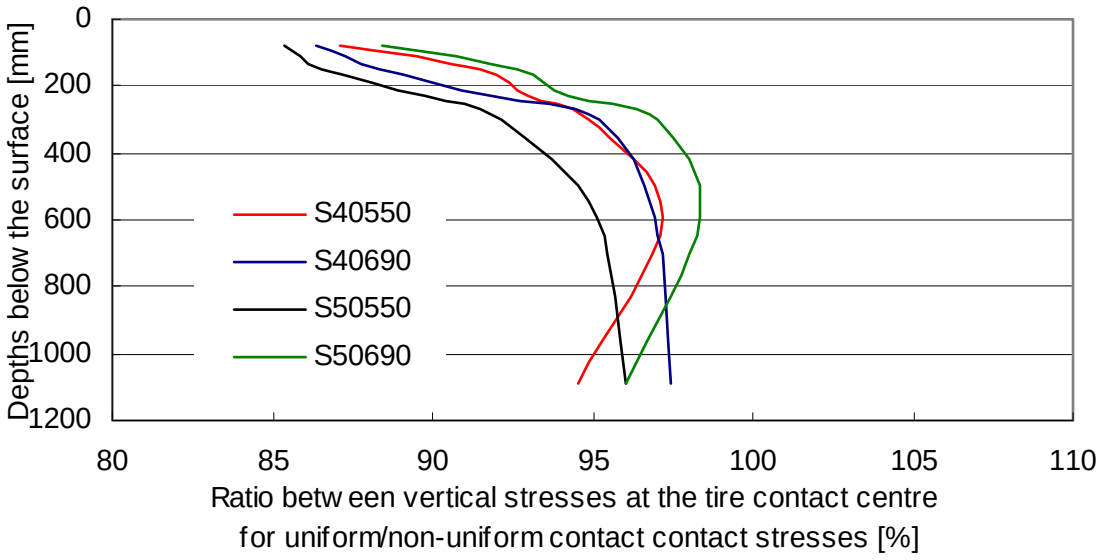

Figure 38 Ratio between vertical stresses at the centre of the tire contact area (inner wheel) versus pavement depths (asphalt layer magnitudes are not displayed) – dual tyre.

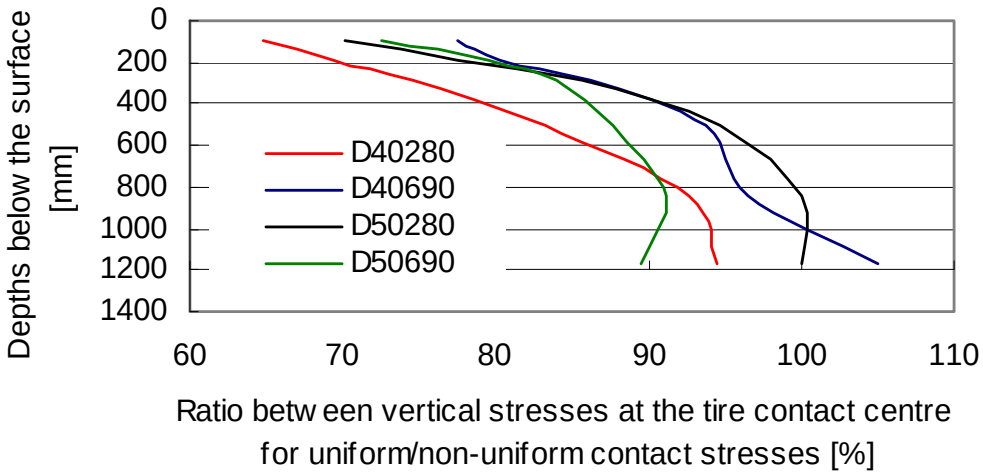

4.3 Vertical elastic strain distribution

Figure 39 shows the vertical elastic strain distribution in the pavement under a 40kN loaded single wheel assuming a uniform (left) and non-uniform (right) tyre/pavement contact stress distribution. The modelled non-uniform tyre/pavement contact stresses result in higher vertical elastic base course strain magnitudes compared with the results obtained from uniform vertical contact stress. Furthermore, figure 41 illustrates that the most critical (maximum) vertical elastic strains occur at the top of the base course layer (at a depth of about 80mm).

Figure 39 Vertical elastic pavement strains under a 40 kN tyre load with tyre inflation pressure of 690 kPa – uniform vertical contact stress (left) and modelled vertical, transverse, and longitudinal stresses (right)

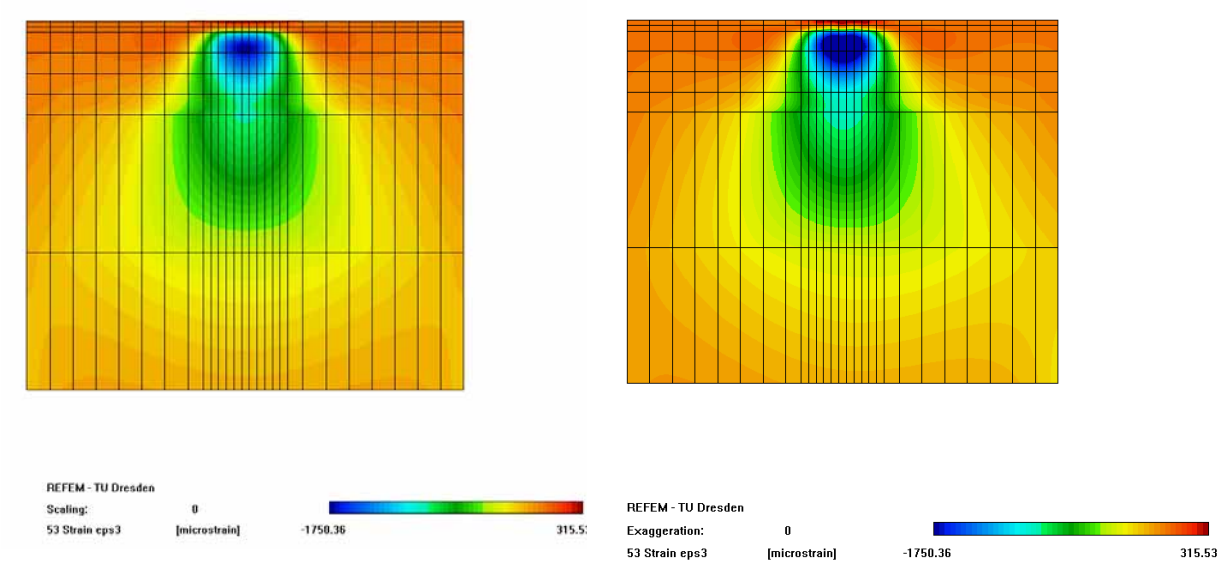

Figure 40 illustrates the vertical elastic strain distribution in the pavement under a 40kN loaded dual wheel configuration assuming a uniform (left) and non-uniform (right) tyre/pavement contact stress distribution. The modelled non-uniform tyre/pavement contact stresses result in higher vertical elastic base course strain magnitudes under the inner wheel compared with the results obtained from uniform vertical contact stress. Much lower strain values will develop in the base course under the outer wheel assuming a non-uniform compared to a uniform tyre/pavement contact stress distribution. It is thought this was due to the particulars of the alignment of the dual wheel (camber, toe-in angle), because the wheels were following a circular path, and/or due to possible differences in the tyres on the dual wheel (no two tyres are identical.

Figure 40 Vertical elastic pavement strains under a 40 kN dual tyre load with tyre inflation pressure of 690 kPa – uniform vertical contact pressure (left) and modelled vertical, transverse, and longitudinal contact stresses (right)

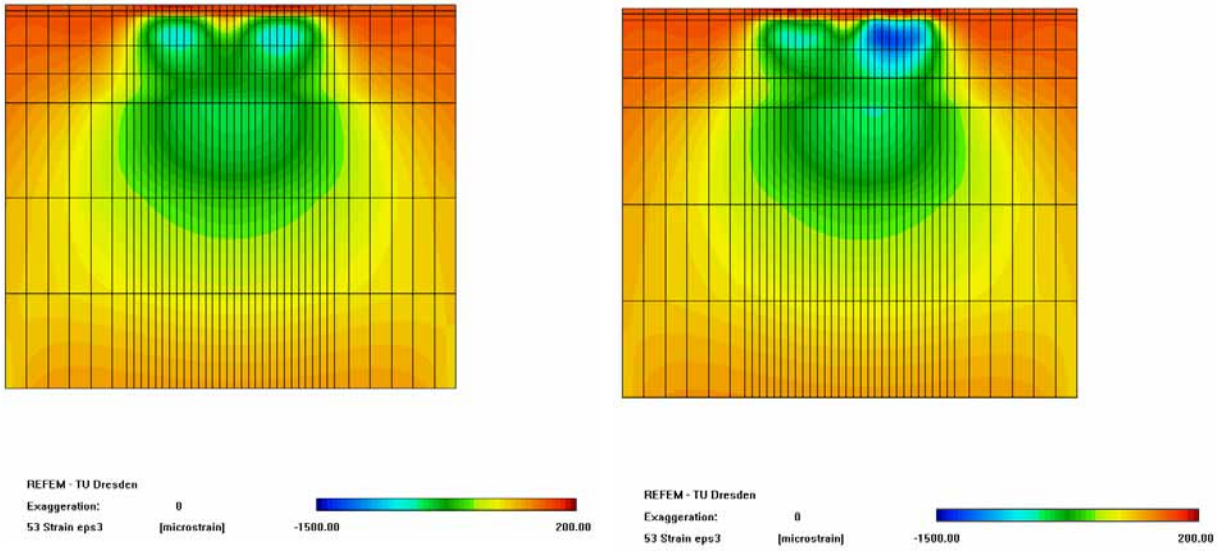

The vertical elastic pavement strains under single wheels determined assuming a uniform and non-uniform contact stress distributions are compared in figure 41. The difference between the calculated vertical elastic strains in the base course is significant. In particular, the results from the FE analysis showed that contact pressure distribution influences the predicted strains within the top 250mm of the pavement modelled. As indicated in figure 41, at greater depths the differences between the two approaches become insignificant. By comparing the vertical strain values under a dual and a single wheel (figure 41 and figure 42), it is clear that for the same loading and the tyre inflation pressures significantly higher stresses and strains will be induced the pavement by a single wheel. In addition, figure 42 shows that the most critical (maximum) vertical elastic strains occur at the top of the base course layer for all loading configurations investigated. For the dual wheels, the measured non-uniform contact stress causes higher strain than the uniform contact stress.

Figure 41 Vertical strains at the centre of the tyre contact area versus pavement depths – single wheel

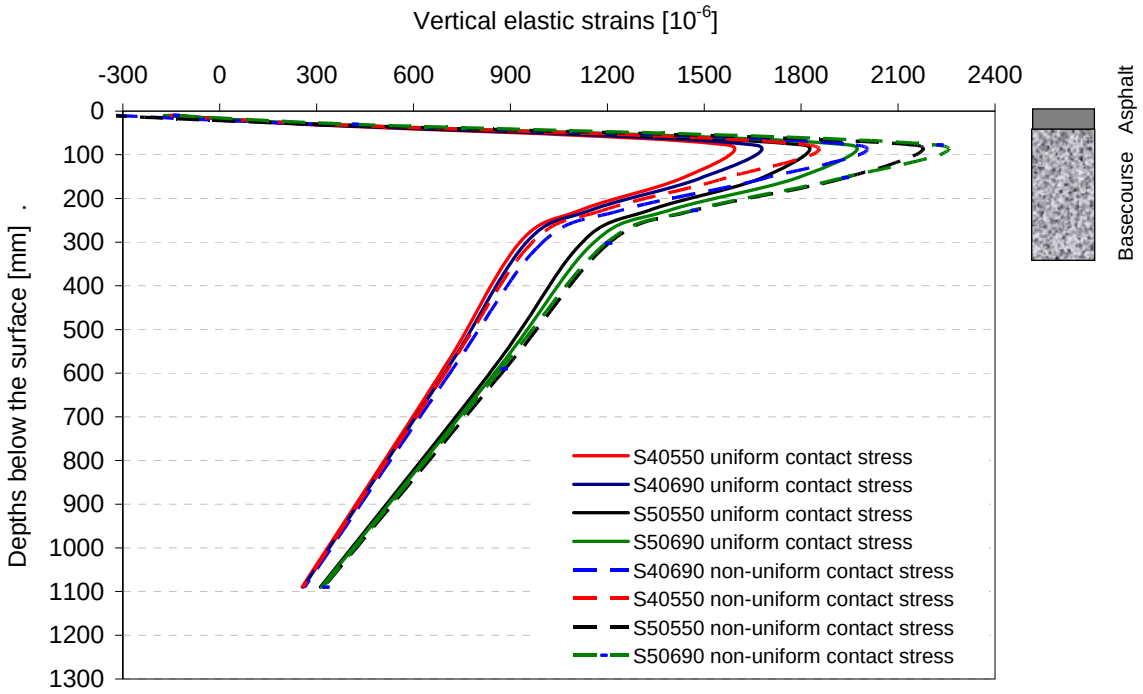

Figure 42 Vertical strains at the centre of the tyre contact area versus pavement depths – dual tyre

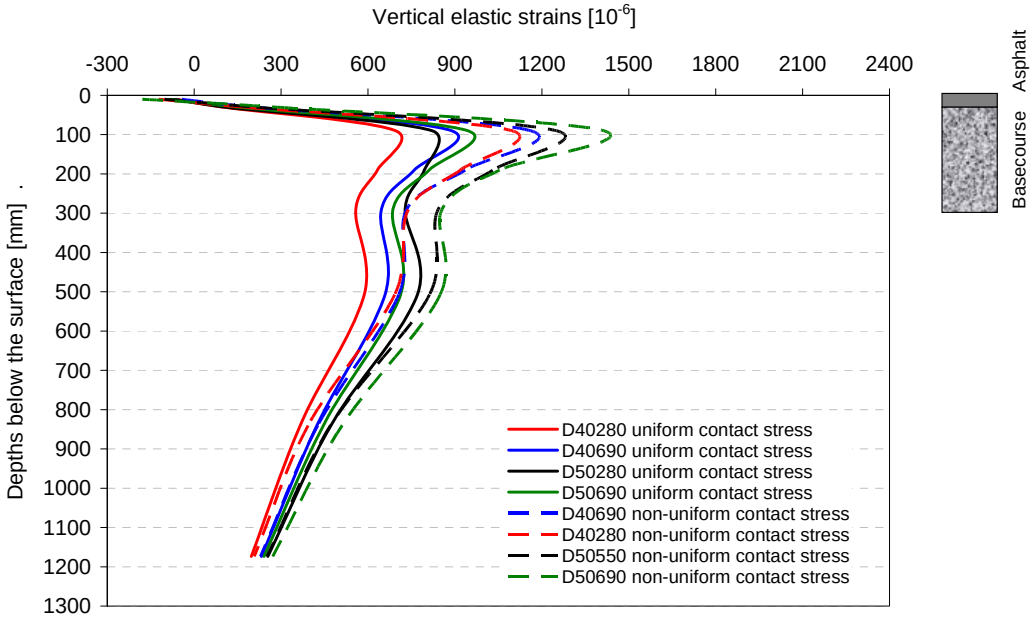

A very interesting observation was that with decreasing tyre inflation pressures and decreasing wheel loads (D40_280) the difference between tyre contact pressures between the two tyres of the dual wheel become bigger. On the other hand, for the tyre configuration D50690 very similar contact pressures

under the two tyres were measured and hence similar stresses and strain magnitudes induced by the two tyres were calculated.

Figure 43 Vertical strain ratio between the inner and outer wheel versus pavement depths – dual tyre

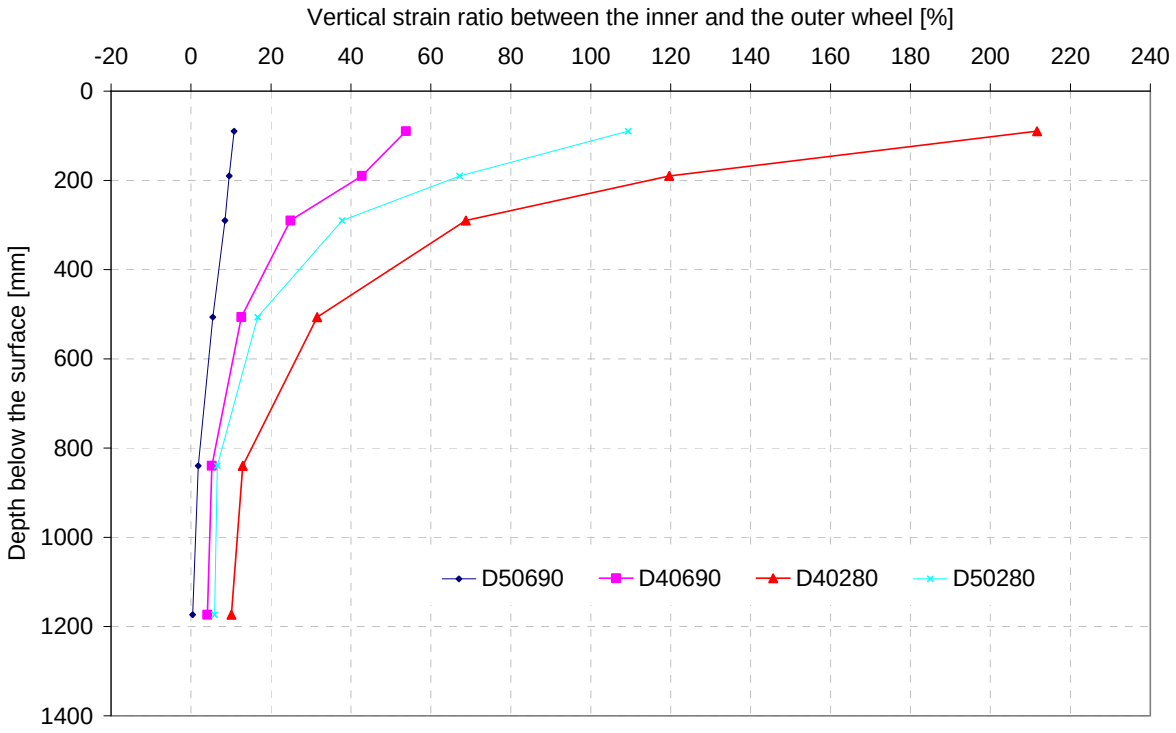

4.4 Vertical surface displacement

A more demonstrative picture of the effect of the uniform and non-uniform contact stress distribution on the pavement performance given in figures 44 and 45. For the non-uniform tyre/pavement contact stress higher elastic surface deflection magnitudes were calculated compared with the results obtained assuming uniform vertical contact stress.

Figure 44 Vertical elastic pavement deformation under a single tyre for a 40kN wheel load with tyre inflation pressure of 690kPa – uniform vertical contact pressure (left) and modelled vertical, transverse, and longitudinal contact pressure (right)

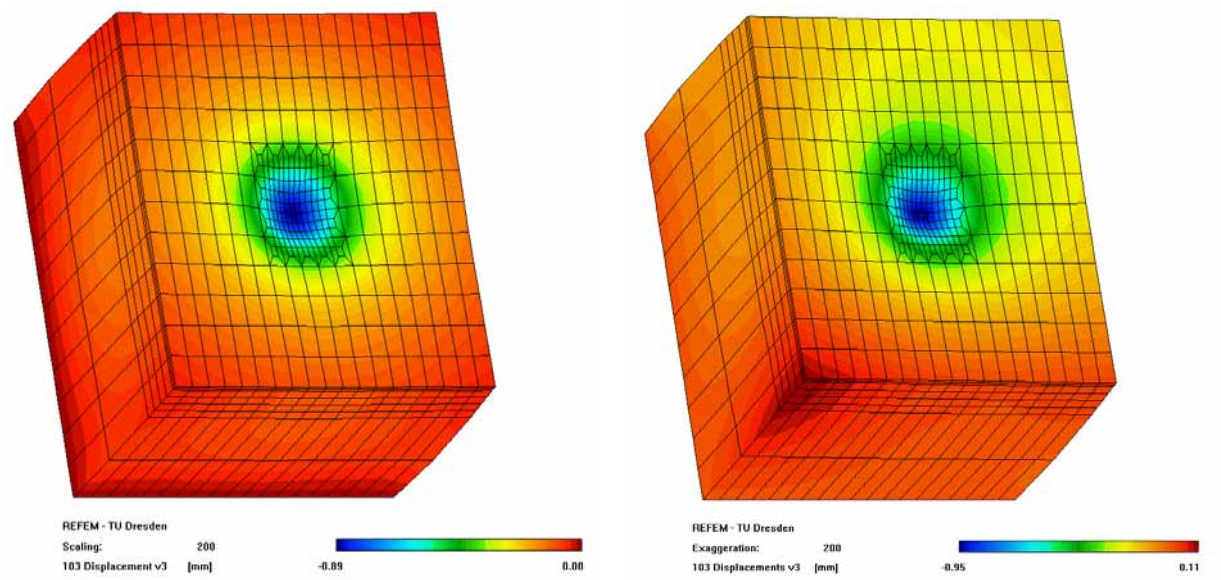

Figure 45 illustrates the higher deflection under the outer wheel compared to the inner wheel for the modelled non-uniform contact stress distribution.

Figure 45 Vertical elastic pavement deformation under a dual tyre for a 40kN wheel load with tyre inflation pressure of 690kPa – uniform vertical contact pressure (left) and modelled vertical, transverse, and longitudinal contact pressure (right)

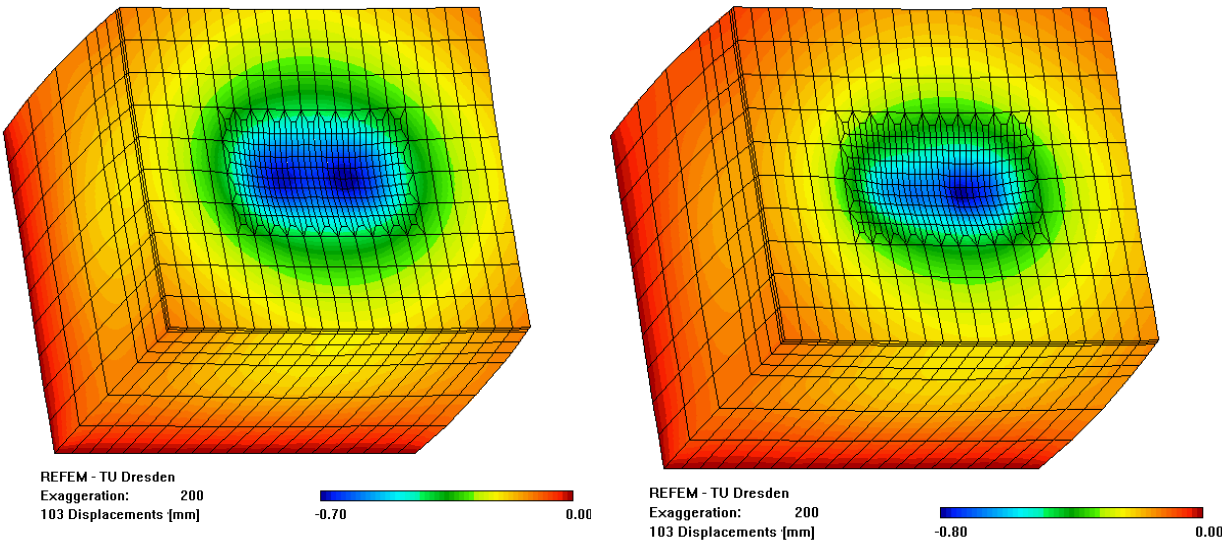

For inner (right) wheel of the dual tyre configuration, the non-uniform tyre/pavement contact stress resulted always in higher elastic surface deflections compared with the results obtained from uniform vertical contact stresses. This was, however, not the case for the outer (left) wheel of the dual tyres. It

is thought this was due to the particulars of the alignment of the dual wheel (camber, toe-in angle), because the wheels were following a circular path, and/or due to possible differences in the tyres on the dual wheel (no two tyres are identical).

Figure 46 shows that for the single tyre contact stress distributions investigated greater elastic pavement deflections were obtained for the non-uniform contact stresses compared to uniform contact stresses. As would be expected, higher wheel loads produce higher deflections and greater tyre inflation pressures also produce greater deflections.

Figure 46 Vertical elastic surface deflection at the centre of the tyre contact area versus pavement depths

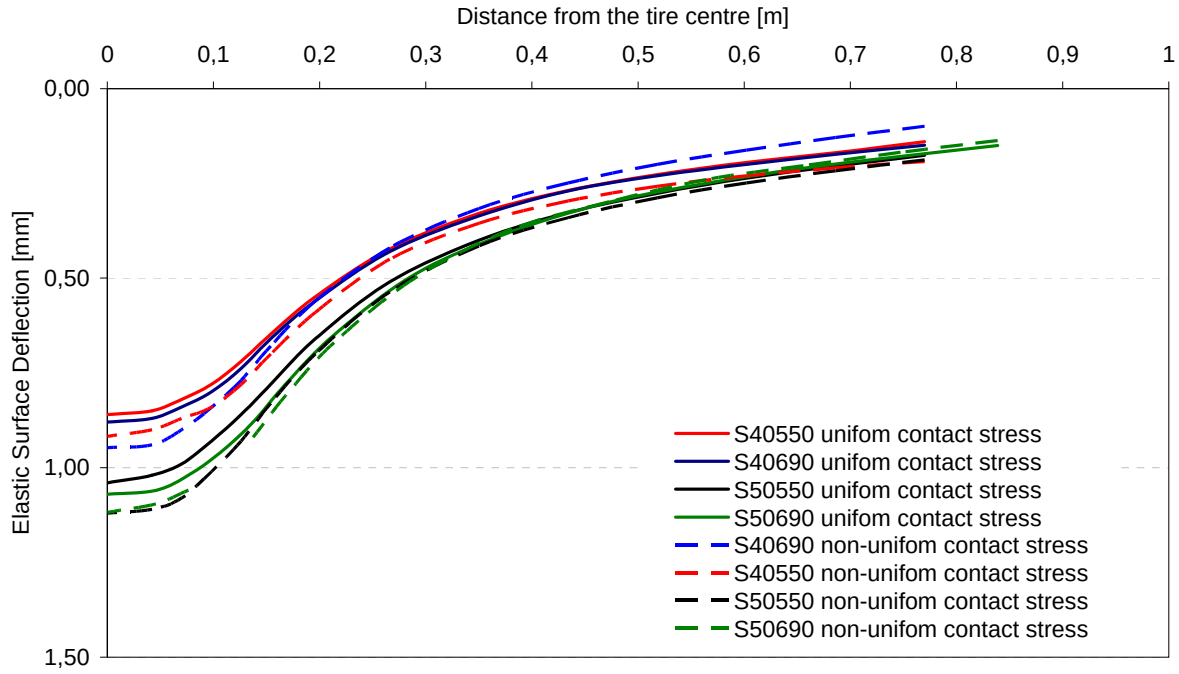

4.5 Shear stress distribution

Shear failure is possible within granular layers whereby small lateral translation of the aggregate is caused by unequal strains in different directions. This involves the aggregate being horizontally translated due to the applied loads. Particle rearrangement is possible. This can result in plastic deformation and rutting. Figures 47 and 48 illustrate the plots of the shear stresses $\sigma_{2/3}$ predicted by the FE model. The model shows that the shear stress magnitudes are relatively small. As illustrated in figures 47 and 48 at the front of the tyre shear stress in positive direction and at the back of the tyre shear stresses in negative direction will be induced in the pavement. A similar shear stress distribution resulted; however, naturally lower shear stress magnitudes were determined in the pavement for the dual tyre configuration. As expected, the highest shear stress magnitudes were calculated for the asphalt layer.

Figure 47 Vertical shear stresses in the longitudinal (fore-and-aft) plane under a single tyre with a 40kN wheel load and tyre inflation pressure of 690kPa through the wheel centreline - uniform vertical contact stress (left) and modelled non-uniform contact stress (right)

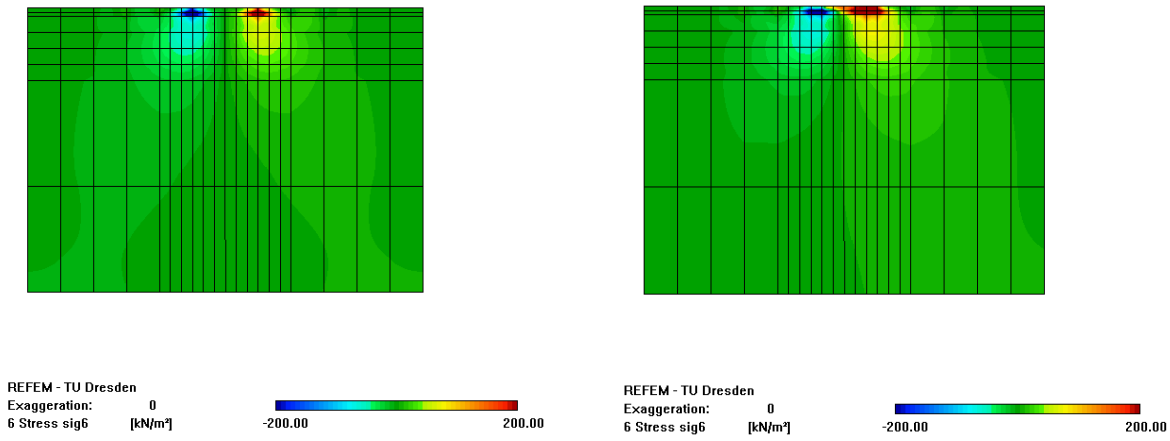

Figure 48 Vertical shear stresses in the longitudinal (fore-and-aft) plane under a dual tyre with a 40kN wheel load and tyre inflation pressure of 690kPa through the wheel centerline – uniform vertical contact stress (left) and modelled non-uniform contact stress (right)

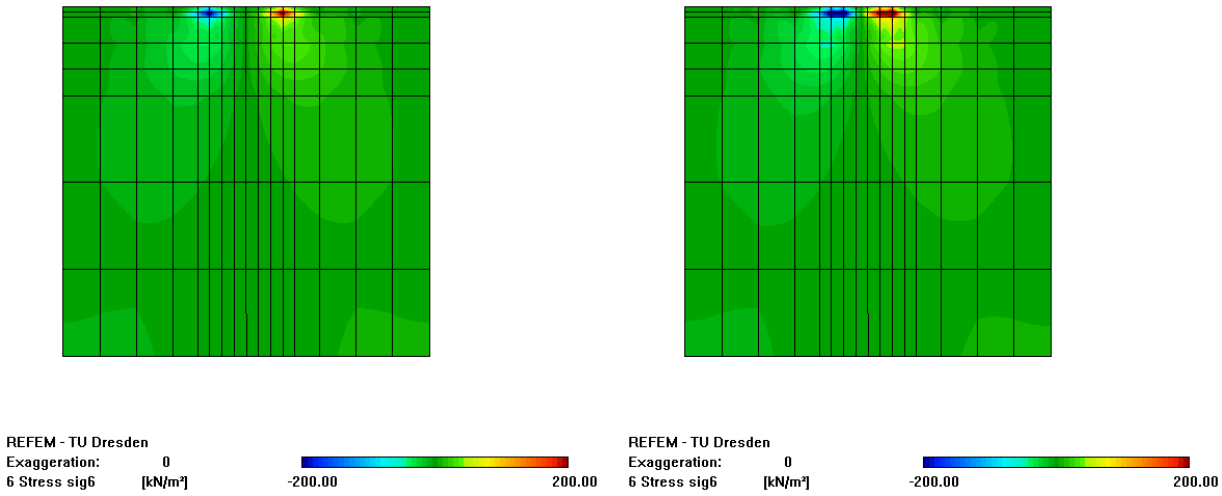

4.6 Shear strain distribution

Hayward (2006) investigated whether the shear strains are related to plastic deformation. The research showed that there was a strong relationship between the magnitude of the basecourse shear strain and the rut depth at the end of the post-construction compaction period. The investigation also showed that shear strain magnitudes in the region of 5000με result in rapid shear failure in the granular layer. Because the shear strain magnitudes are closely related to the development of rutting, the shear strains were analysed as well within this project.

Figures 49 and 50 illustrate the shear strain in the longitudinal plane under a single and dual tyre. It can be seen that the highest shear strains occur in the basecourse for the pavements investigated. In

general, the shear strain magnitudes are higher in the pavement loaded by a single wheel compared to the pavements loaded by a dual wheel. For the non-uniform tyre/pavement contact stress higher shear strain magnitudes were calculated under the inner dual wheel compared with the results obtained from uniform vertical contact stress (figure 50).

Figure 49 Vertical shear strains in the longitudinal plane under a single tyre with a 40kN wheel load and tyre inflation pressure of 690kPa through the wheel centerline - uniform vertical contact stress (left) and modelled non-uniform contact stress (right)

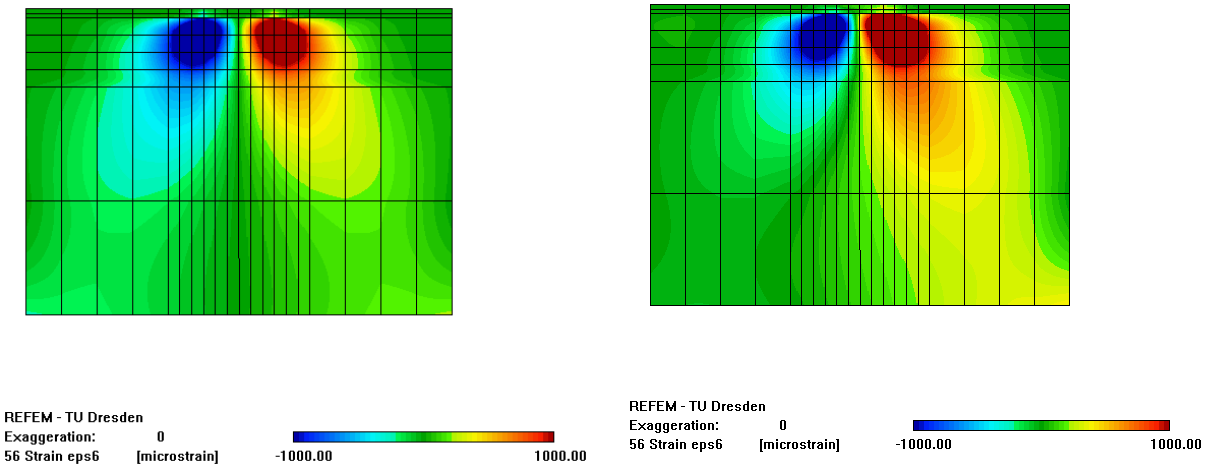

Figure 50 Vertical shear strains in the longitudinal plane under a dual tyre with a 40kN wheel load and tyre inflation pressure of 690kPa through the wheel centerline - uniform vertical contact stress (left) and modelled non-uniform contact stress (right)

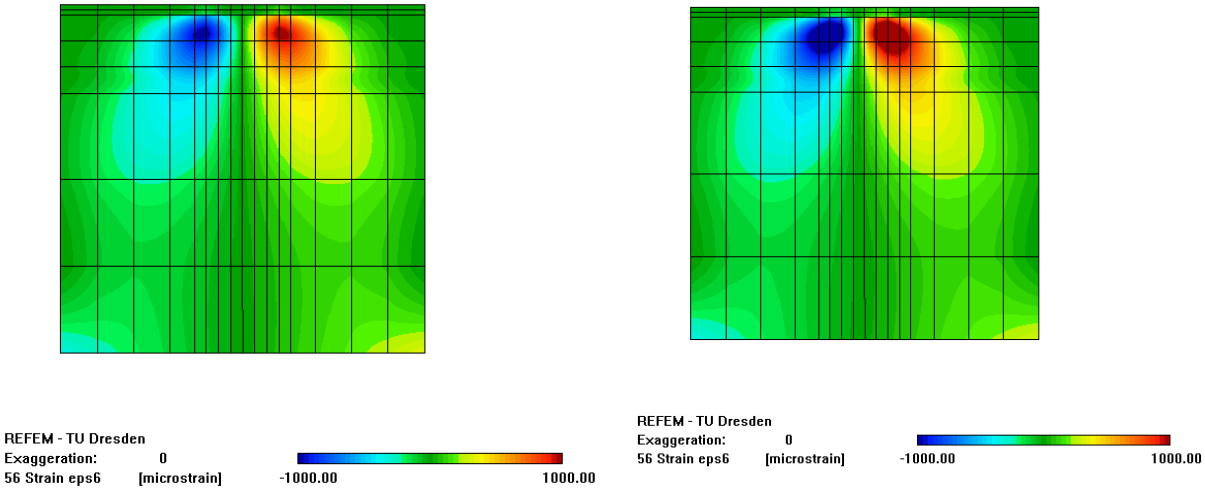

5 Rut depth calculations

For thin pavements, the base course is vitally important to withstand induced strains which could cause premature failure. To evaluate the rutting risk of the base course, the vertical elastic pavement strains were analysed at the centre of the tyre /pavement contact area. Werkmeister (2007) developed an approach to predict the plastic deformation of the base course in pavements based on elastic pavement strain values. The investigation is based on RLT test results and uses the vertical elastic strain to predict the vertical plastic strain rate per load cycle. The relationship is applied to the vertical elastic strains calculated earlier and integrated over the depth of the base course layer and a defined number of load cycles to determine the total plastic deformation (rut depth) occurring in the base course. RLT strain tests were conducted on a typical New Zealand base course material (Pound's Road greywacke). The material was tested at 95% DOC and at 70% of OMC.

5.1 Plastic strain calculation

The raw RLT test data were analyzed in terms of vertical elastic strain (ε_{el}) and the plastic strain rate ($\dot{\varepsilon}_p$) (see figure 51). Because the initial part of the plastic deformation curve is often influenced by the technique used in preparing the sample, it was decided to focus on the steady state response of the sample (load cycles 20,000 to 50,000).

The elastic strain value (ε_{el}) was averaged over the same interval to give an average value of ε_{el}. The following exponential relationship (Equation 3) between the elastic strain (ε_{el}) and plastic strain rate ($\dot{\varepsilon}_p$) can be determined.

$$\dot{\varepsilon}_p = a \cdot \dot{\varepsilon}_{el}^{\ b} \tag{3}$$

where:

$\dot{\varepsilon}_p$ [10^{-3}/load cycle] major principal plastic strain rate per load cycle,

$\dot{\varepsilon}_{el}$ [10^{-3}/load cycle] major principal elastic strain rate per load cycle,

a, b [-] material parameters.

Figure 51 shows the relationship between axial elastic strain and axial plastic strain rate per load cycle on a (ε_{el}) vs. ($\dot{\varepsilon}_p$) plot.

Figure 51 Plastic strain rate per load cycle versus elastic strain rate per load cycle for the Greywacke at 95% DoC, RLT test results

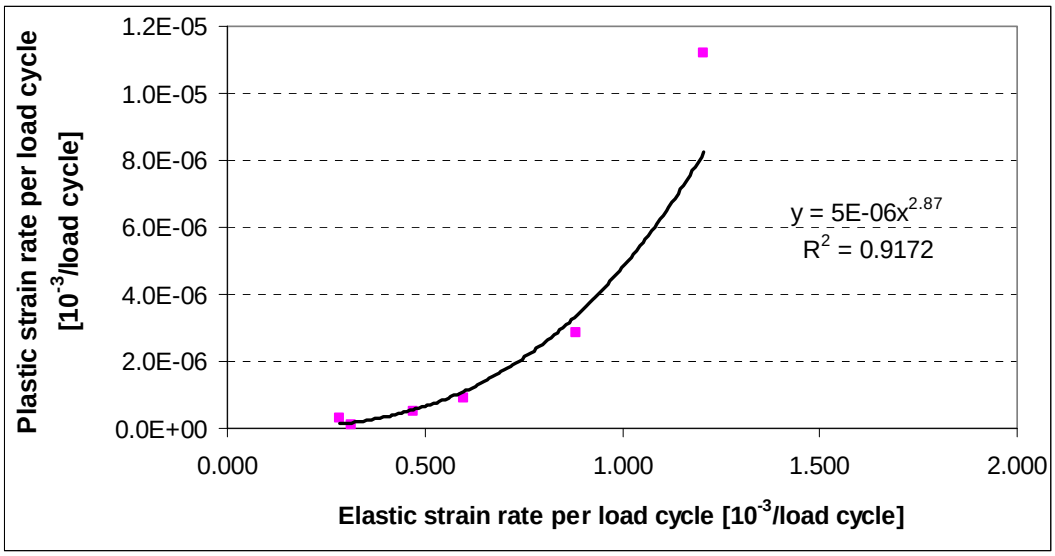

5.2 Base course rut depth calculations

The development of plastic deformation for thin surfaced pavement can be divided into the initial post-construction compaction caused by traffic and the steady state phase. The initial post-construction compaction for thin surfaced pavements is usually completed within the first 25,000 to 100,000 load cycles. The amount of plastic deformation that occurred from the first loading of the pavement to the completion of post-construction compaction phase, and the plastic deformation that occurred from the completion of post-construction compaction phase to a defined number of load cycles, were calculated.

As already mentioned, the vertical elastic strain profiles of the pavements were determined at the centre of the tyre contact areas for the loads applied in the CAPTIF tests using FE calculation results. The base course layer was divided into a number of sublayers and the axial elastic strain values at the mid points of the layers were used to determine the value of the plastic strain rate ($\dot{\varepsilon}_p$) for each layer. Finally, the plastic deformation of the base course was determined by multiplying each plastic strain rate value ($\dot{\varepsilon}_p$) by the sublayer thickness and the number of load cycles. The total amount of plastic deformation of the base course layer was calculated by summing the contributions of each sublayer. For table 18 and table 19 the steady state plastic strain rate is calculated using equation 4:

$$\dot{\varepsilon}_p = 5 \times 10^{-6} \dot{\varepsilon}_{el}^{2.87} \quad (4)$$

The plastic deformation for steady state plastic strain is calculated using Equation 5

$$v_p = \dot{\varepsilon}_p h N \quad (5)$$

The load cycles to the end of post-construction compaction phase are calculated using Equation 6

$$N_{pc} = 211.71 \dot{\varepsilon}_{el}^{0.8232} \dot{\varepsilon}_{ppc} = 0.0042 \cdot \dot{\varepsilon}_p^{\,1-0.6869} \quad (6)$$

$$\dot{\varepsilon}_{pcc} = 0.0042 \cdot \dot{\varepsilon}_p^{\,1-0.6869} \quad (7)$$

$$v_p cc = \dot{\varepsilon}_{pcc} h N \quad (8)$$

Tables 18 and 19 show the magnitudes for the base course deformations assuming a DoC of 95% for the base course.

Table 18 Plastic deformation of the base course assuming a uniform contact pressure distribution, 40kN load and 690kPa tyre inflation pressure

Depth to midheight of the sublayer	Sublayer thickness	Elastic strains	Plastic strain rate steady state	Plastic deformation steady state	Load cycles post-construction compaction	Plastic strain rate post-construction compaction	Plastic deformation during post-construction compaction phase
[mm]	[mm]	[10^{-3}]	[10^{-3}/cycle]	[mm]	[-]	[10^{-3}/cycle]	[mm]
77.5	75	1.66	2.12E-05	1.44	94505	1.45E-04	1.02
152.5	75	1.49	1.57E-05	1.08	86726	1.32E-04	0.86
227.5	75	1.15	7.39E-06	0.52	69833	1.04E-04	0.54
302.5	75	0.95	4.28E-06	0.30	59686	8.75E-05	0.39
Plastic base course deformation after 1 x 10^6 load cycles [mm]				3.34			2.82
Total deformation 3.34+2.82 = 6.15mm							

Table 19 Plastic deformation of the base course assuming a non-uniform contact pressure distribution, 40kN wheel load and 690kPa tyre inflation pressure

Depth to mid-height of the sublayer	Sublayer thickness	Elastic strains	Plastic strain rate steady state	Plastic deformation steady state	Load cycles post-construction compaction	Plastic strain rate post-construction compaction	Plastic deformation during post-construction compaction phase
[mm]	[mm]	[10-3]	[10-3/cycle]	[mm]	[-]	[10-3/cycle]	[mm]
77.5	75	1.97	3.50E-05	2.34	109080	1.69E-04	1.38
152.5	75	1.69	2.27E-05	1.54	96288	1.48E-04	1.07
227.5	75	1.24	9.27E-06	0.64	74515	1.12E-04	0.62
302.5	75	1.00	4.94E-06	0.35	62217	9.16E-05	0.43
Plastic base course deformation after 1 x 10^6 load cycles [mm]				4.87			3.50
Total deformation 4.87+3.50 = 8.37mm							

In terms of the predicted base course rutting derived from the elastic strains, the results showed for the single tyre and inner wheel of the dual tyre arrangement, significantly higher plastic deformations were predicted for the non-uniform contact pressure. This is displayed graphically in figure 52. However, lower plastic base course deformation due to the lower loading of one of the tyres of the unequally-loaded dual tyres is predicted for three out of four experiments (D40280, D40690 and D50280) for a non-uniform tyre/pavement contact stress distribution. If the dual tyres were

approximately equally loaded (D50690) the predicted rutting under both wheels was significantly greater for the non-uniform contact pressure (figure 52).

Figure 52 Comparison of predicted base course rutting

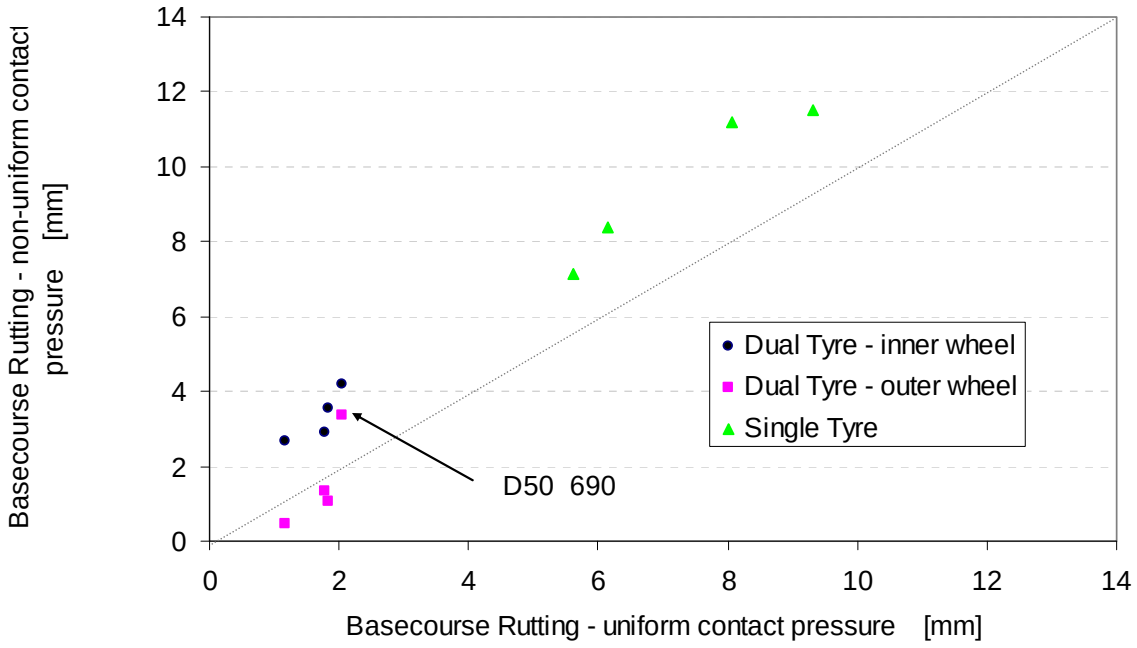

6 Conclusions

In this research, a three-dimensional (3-D) Finite Element (FE) model was used to compare the predicted pavement response and performance for non-uniform tyre/pavement contact stress distributions with the response and performance for uniform contact stress distributions. The stress and strain distributions were used to identify the differences in the pavement response to the two loading configurations, and predicted rutting was used to compare performance. The pavement modelled had a thin, non-structural asphalt surface and a 300mm base course. For the FE modelling, element forces were applied in the vertical, longitudinal and transverse directions. These element forces were derived from measurements made at Transit NZ's CAPTIF indoor, full-scale test facility in Christchurch, New Zealand. This approach permitted the FE model to use more realistic non-uniform loading forces representative of those applied by real tyres. It should be kept in mind that the horizontal tyre/pavement contact stress distributions measured at CAPTIF were generated by self-driven wheels travelling around a curve of constant 9m radius.

Based on the results of the FE calculations the following conclusions can be drawn:

- The non-uniform tyre/pavement contact stresses result in more concentrated stress distributions in the asphalt layer and the base course of the pavement when compared to the results obtained from uniform vertical contact stresses. In particular, the results from the FE analysis showed that the contact pressure distribution influenced the predicted stress within the top 250 mm of the thin pavement. This finding indicated that the effects of differences in tyre contact stress distributions are mainly were seen near the pavement surface and diminished with depth.

- Comparisons derived from the 3D FE analyses showed that the differences in the elastic strain values were insignificant in the subgrade for the uniform and non-uniform contact stresses applied to the thin pavement investigated. However, the differences in the elastic strain values in the base course and the asphalt layer were significant when the effects of the uniform and non-uniform contact stresses were compared.
- For single and dual tyres (inner wheel), the non-uniform tyre/pavement contact stress resulted in higher elastic surface deflections compared with the results obtained from uniform vertical contact stresses. This was, however, not the case for the outer wheel of the dual tyres. It is thought this was due to the particulars of the alignment of the dual wheel (camber, toe-in angle), because the wheels were following a circular path, and/or due to possible differences in the tyres on the dual wheel (no two tyres are identical).
- The result of the FE calculation does imply that tyre contact pressure distributions have a major effect on stress and strain distributions in the asphalt layer and the base course and only minor effect on the subgrade values of thin surfaced pavements. Hence, the tyre contact stress distribution will influence the development of rutting in the layers near the surface.
- When applied to the research results, a model of thin surfaced pavement rutting, utilising plastic strain rates derived from elastic strains predicted significantly greater rutting for the real contact stresses as compared to a uniformly distributed contact pressure.
- On the basis of the results of the 3D FE calculation the authors recommend that for thin surfaced pavements the analysis of surface damage such as rutting be made as detailed as possible by modelling the actual tyre loading conditions. If no contact stress measurement data are available, special computer programs (eg developed by Park et al (2005)) or the approaches developed by Groenendijk (1998) can be used to calculate the vertical, longitudinal and transverse tyre/pavement contact stresses.

7 References

Arnold, G (2004) Rutting of granular pavements. Ph.D Thesis, University of Nottingham, Nottingham, United Kingdom.

Bathe, KJ (2002) *Finite element-methods*. Berlin: Springer Verlag.

Blab, R (2001). Analytische Methoden zur Modellierung der Verformungseigenschaften flexibler Fahrbahnaufbaten. Mitteilung nr. 11. Vienna: Technische Universität Wien, Institute für Straßenbau und Straßenerhaltung.

De Beer, M (1996) Measurement of tire/pavement interface stresses under moving wheel loads. Heavy vehicle systems. Special series. *International Journal of Vehicle Design 3,* no.1–4: 97–115.

Douglas, RA, D Alabaster and N Charters (2008) Measured tire/road contact stresses characterized by tire type, wheel load, and inflation pressure. In *Proceedings of 2008 Annual Conference of the Transportation Association of Canada*, Toronto. Proc. available on CD. 12pp.

Gleitz, T (1996) Beitrag zur rechnerischen Erfassung des nichtlinearen Spannungs-Verformungsverhaltens ungebundener Tragschichtmaterialien in flexiblen Straßenkonstruktionen (Non-linear deformation behaviour of unbound granular layers in pavement constructions – in German). Ph.D. Thesis, University of Technology, Dresden.

Groenendijk, J (1998) Accelerated testing and surface cracking of asphaltic concrete pavements. Ph.D. Dissertation, University of Technology. Delft.

Hayward, B (2006) Investigation of road base shear strains using in-situ instrumentation, Master Thesis, University of Canterbury, Christchurch.

Oeser, M (2004) Numerische Simulation des nichtlinearen Verhaltens flexibler mehrschichtiger Verkehrswegebefestigungen, Ph.D. Thesis, University of Technology, Dresden.

Park, DW, E Fernando and J Leidy (2005) Evaluation of predicted pavement response using measure tire contact stresses. CD Annual Meeting Transportation Research Board. Washington DC.

Tielking, JT and FL Roberts (1987) Tire contact pressure and its effect on pavement strain. *Journal of Transportation Engineering 113*, no.1.

Transit New Zealand (TNZ) (2007) Transit New Zealand Standard TNZ T/15 Repeated Load Triaxial (RLT) Testing of Unbound and Modified Road Base Aggregates, owner David Alabaster, status Draft, comment Under Development.

Werkmeister, S (2003) Permanent deformation behaviour of unbound granular materials in pavement constructions, PhD Thesis, University of Technology, Dresden.

Werkmeister, S (2007) *Prediction of pavement response using accelerated test results of New Zealand's CAPTIF Facility.* Dresden: Habilitation, University of Technology.